output-pics.pdf

CHALMERS

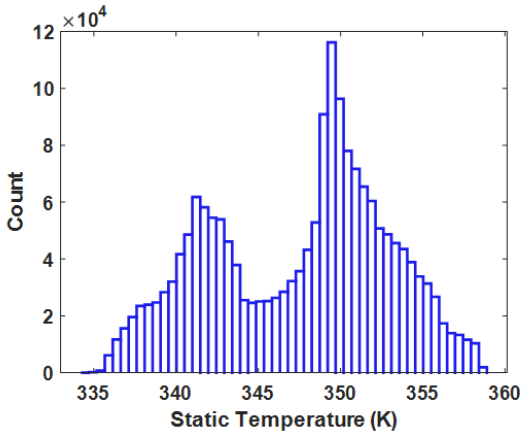

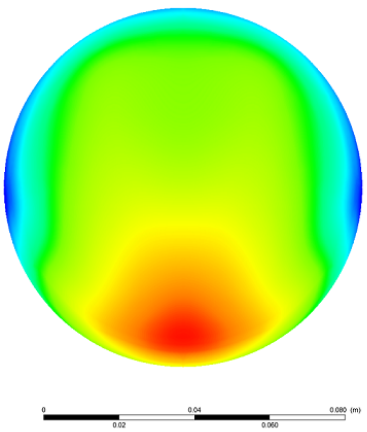

Reduced Order Models For Exhaust AfterTreatment Systems

Coupling Modeling, Simulations and Chemometrics

PRATHEEBA CHANDA NAGARAJAN

Division of Energy Conversion and Propulsion Systems
Department of Mechanics and Maritime Sciences
CHALMERS UNIVERSITY OF TECHNOLOGY
Göteborg, Sweden 2024

THESIS FOR THE DEGREE OF DOCTOR OF PHILOSOPHY IN THERMO AND FLUID DYNAMICS

Reduced Order Models For Exhaust AfterTreatment Systems

Coupling Modeling, Simulations and Chemometrics

PRATHEEBA CHANDA NAGARAJAN

Department of Mechanics and Maritime Sciences
CHALMERS UNIVERSITY OF TECHNOLOGY

Göteborg, Sweden 2024

Reduced Order Models For Exhaust AfterTreatment Systems
Coupling Modeling, Simulations and Chemometrics
PRATHEEBA CHANDA NAGARAJAN
ISBN 978-91-8103-053-2

Doktorsavhandlingar vid Chalmers Tekniska Högskola
Ny serie nr. 5511
ISSN 0346-718X

Division of Energy Conversion and Propulsion Systems
Department of Mechanics and Maritime Sciences
Chalmers University of Technology
SE-412 96 Göteborg
Sweden
Telephone: +46 (0)31-772 1000

Cover Picture: Histogram and Contour of Temperature on the outlet of EATS Catalyst .

Chalmers Reproservice
Göteborg, Sweden 2024

Abstract

The use of hydrocarbon based fuels and the high temperatures generated during combustion processes are major sources of gaseous pollutants that are detrimental to human health and the environment. Emission legislation is increasingly becoming stringent to mitigate the harmful effects of emissions. Exhaust Aftertreatment systems are a group of catalytic devices that convert these harmful emissions into products like carbon dioxide and nitrogen. Space limitation in the exhaust line creates nonuniform flow in terms of flow through bends and dead volumes. This limits the performance of the EATS. The flow from the engine does not proceed uniformly to the EATS, creating a flow maldistribution at the inlet of the EATS. Consequently, velocity, temperature, and concentrations at the exit are influenced by the flow distribution at the inlet.

Accurate models that capture the spatial and temporal variations of the flow distribution in EATS, specifically during cold start conditions and real driving emissions (RDE) tests, are essential to comply with stringent emission standards. 1D and 3D-computational fluid dynamics (3D-CFD) models are used to predict the conversion of species at the exit of EATS. While 1D models are robust, they lack accuracy, whereas, 3D-CFD models offer higher accuracy, but require significant computational resources. This study addresses these challenges primarily through Computational Fluid Dynamics (CFD) simulations and proposes a methodology for developing reduced-order models.

Firstly, characterizing and quantifying flow distribution in EATS under transient conditions with realistic geometry is performed using non-reactive simulations. Flow uniformity index is used to characterize the extent of variation of the flow parameters in any catalyst plane. In addition to the uniformity index, contours and histograms are employed to demonstrate the non-uniform flow field.

The effect of inlet pulsations on the mixed cup conversion at exit of catalyst is studied using transient reactive simulations. Four transient inlet profiles, *viz.,* constant flowrate, sinusoidal, rectangular, and triangular pulse profiles, are chosen to describe the inlet pulsations. The results show that the fluctuations and pulsations in the incoming flow to a monolithic reactor in an aftertreatment system, affect both the transient response of the reactor as well as its time-averaged performance. The method of specifying the inlet boundary conditions also influences the solutions.

A methodology for developing a reduced-order model by combining physics-based CFD solutions with multivariate data analysis methods is proposed. This method is demonstrated by combining CFD solutions of transient reactive simulations on a diesel oxidation catalyst with chemometric techniques. Performance evaluations validate the efficacy of the multi-channel model over single-channel models. Computational efforts for creating the multichannel model are comparable to single-channel models, when utilizing available CFD data and coupling chemometrics analysis. This enables rigorous control applications with improved accuracy. The methodology can be extended to real-world emissions aftertreatment systems with complex geometries.

Further, predictions of species conversions in systems with flow maldistribution are made by performing steady state reactive 3D-CFD simulations and mapping the same with 1D-SCM. A pseudo-channel is envisaged that provides the same species conversion as the 3D-CFD, by formulating an objective function, which is the difference of species conversions of 3D-CFD and 1D-SCM. The error of the objective function is minimized by iteratively varying the velocity that will provide the same conversion in a 1D-SCM. The pseudo-channel model outputs agree closely with the CFD results in various steady-state and transient test cases.

Detached eddy simulations were carried out under nonreactive conditions on the geometry with bends to confirm the validity of RANS simulations, as RANS simulations are computationally more effective than DES. Flow uniformity indices were of the same order in both cases, however, DES showed fluctuations.

This thesis aims at developing reduced order models combining CFD simulations and regression and chemometric techniques. It also highlights the limitations of a single channel model in a realistic geometry case. The thesis also attempts to predict species conversion of transient reactive simulations, from the solution of steady state reactive simulations, as the former is computationally more expensive than the latter. The developed pseudo-channel model and multi-channel model can be used for realtime monitoring and control applications. These two methodologies require a computational load comparable to that of 1D models. Validation of these models using EATS experiments under transient conditions is recommended for future research.

Keywords: Exhaust AfterTreatment Systems, CFD Simulations, Flow maldistribution, Transient, Uniformity index, Catalyst, Reactive flows, Single channel model, Multi-channel model, Principal component Analysis, D-Optimal design, Weighted least squares, Nonlinear least squares optimization

List of publications

This thesis is based on the work presented in the following papers, which are referred to throughout the text by their Roman numerals:

I. **Transient flow uniformity evolution in realistic exhaust gas aftertreatment systems using 3D-CFD**
P. Chanda Nagarajan, H. Ström and J. Sjöblom.
Emission Control Science and Technology **8(3)** (2022) 154-170

II. **Numerical assessment of flow pulsation effects on reactant conversion in automotive monolithic reactors**
P. Chanda Nagarajan, H. Ström and J. Sjöblom.
Catalysts **12(6)** (2022) 613

III. **Turbulent uniformity fluctuations in automotive catalysts – A RANS vs DES assessment**
P. Chanda Nagarajan, J. Larsson, O. Tylén, A. Murali, A. Larsson, E. Peyvandi, S. Rangaswamy, H. Ström and J. Sjöblom.
Results in Engineering **16** (2022) 100772

IV. **Methodology for reduced-order multi-channel modeling of a catalytic converter**
P. Chanda Nagarajan, H. Ström and J. Sjöblom.
Submitted to *Industrial & Engineering Chemistry and Research*

V. **A reduced-order pseudo-channel model accounting for flow maldistribution in automotive catalysis**
P. Chanda Nagarajan, H. Ström and J. Sjöblom.
In manuscript

Acknowledgements

This is a very special moment for me, and I would like to thank people who have helped me to make it possible. Firstly, I would like to thank my advisors Jonas Sjöblom and Henrik Ström for all their advice, support, and guidance over the last five years. Their complementary perspectives, one rooted in experimental rigor and chemometrics and the other in CFD modeling techniques, have enriched my research experience enriching my academic journey in ways I could not have imagined. Our weekly meetings and discussions were so refreshing with constructive discussions, meaningful insights and loads of laughter. Jonas, thank you so much for giving me the opportunity believing in me. I would like to inherit your optimism and enthusiasm. Whenever I came with questions, doubts and thoughts, and my anxieties, you had time for all of them. Another important thing to learn from you: Your interest and effort in explaining things, both within academics and outside, helping me learn swedish better, and being so open to discussions. Henrik, thank you so much for being an amazing advisor and mentor. Your words made a world of difference in very challenging times. Thank you! Thank you for giving me the space to discuss several things from coding to Indian classical music, and being very inclusive. I am mesmerized by the clarity in explaining the concepts, elegance in coding and helping me whenever I hit a dead end. I don't think I could have progressed as far as I have without your support and motivation. I feel very privileged to have you as my mentor.

I would like to acknowledge gratefully the funding from CERC and Chalmers. My sincere thanks to Ingemaar, Lucien and members of CERC Reference group meetings. I thank Srdjan Sasic and Derek Creaser for their counsel in the study plan meetings. Thank you so much, Srdjan, for checking on me and providing support in my very difficult times. I thank Rob Thomson for his help and motivation.

My colleagues at the division of ECaPS have always supported me and helped me in multiple ways. Thank you Petter, David, Andrei, Mats, Patrik, Robert, Tim, Anders, Kjell, Anders and Alf. Thank you all, for the happy fika times, discussions filled with information and laughter.

I fall short of words to express my gratitude to Magnus, my former officemate and colleague. Thank you so much for reminding me to care about my wellness.

I would like to thank Elenor and Malin for helping me with various things in the department. You made my life much easier. I thank my colleagues Sreelekha, Vignesh, Mindaugas, Mohammad, Nidal, Abhilash, Victor, Lokesh, Yu, Mina, Lahari, Christian and Nazanin for fun times during lunch and *fika* and creating a wonderful workplace. Wishing you all the very best. My special thanks to Nikhil for making life easier when I started in August 2019. I would like to thank Sudharsan and Sindhuja for all their help and the many lunch and dinners. I would like to thank my buddies Tejaswi, Hari, Volga, Abu, Sindhu, for coming to my rescue everytime. My sincere thanks Dr Balasubramanian, Dr Perarasu and Pravina for being a source of motivation.

I would like to thank my parents, Nagarajan and Chanda, for all the love and care you showered on me. You have always stood by me and supported all my decisions. My siblings, Savithri and Shrenivas have held me up in my most difficult times. I thank Harini and my nephews Achyuth and Kuttipillu, for sharing their love. Thank You Santhosh, Aiswarya, Vasudha and Guruprasad, for the affection and care you shower on me. I thank my uncles and aunts for their affection for me.

Pratheeba

Gothenburg
May 2024.

In The Fond Memory of
My father ***C R Nagarajan***
I regret for not completing this work sooner

and

To
My Family and My Advisors
Thank you for showing me that hope is the best of good things!

Contents

List of Figures

List of Tables

Nomenclature

Abbreviations

1D	**1 D**imensional
3D	**3 D**imensional
ASC	**A**mmonia **S**lip **C**atalyst
CARB	**C**alifornia **A**ir **R**esources **B**oard
CDR	**C**onvection **D**iffusion **R**eaction
CFD	**C**omputational **F**luid **D**ynamics
COPD	**C**ompulsory **O**bstructive **P**ulmonary **D**isorder
CPSI	**C**ells **P**er **S**quare **I**nch
DAE	**D**ifferential **A**lgebraic **E**quations
DES	**D**etached **E**ddy **S**imulations
DNS	**D**irect **N**umerical **S**imulations
DOC	**D**iesel **O**xidation **C**atalyst
DPF	**D**iesel **P**articulate **F**ilter
EATS	**E**xhaust **A**fter**T**reatment **S**ystems
EGR	**E**xhaust **G**as **R**ecirculation
EU	**E**uropean **U**nion
FDM	**F**inite **D**ifference **M**ethod
FEM	**F**inite **E**lement **M**ethod
FVM	**F**inite **V**olume **M**ethod
GHG	**G**reen **H**ouse **G**as
GHSV	**G**as **H**ourly **S**pace **V**elocity
GPF	**G**asoline **P**articulate **F**ilter
HC	**H**ydro**C**arbon
ICE	**I**nternal **C**ombustion **E**ngine
LIF	**L**aser **I**nduced **F**luorescence
MCM	**M**ulti-**C**hannel **M**odel
MFC	**M**ass **F**low**C**ontrollers
MLR	**M**ultiple **L**inear **R**egression
MUSCL	**M**onotonic **U**pstream-centered **S**cheme for **C**onservation **L**aws
MVDA	**M**ulti **V**ariate **D**ata **A**nalysis
NEE	**N**on **E**xhaust **E**missions

NURBS **N**on **U**niform **R**ational **B**- **S**plines

OBD **O**n-**B**oard **D**iagnostics

ODE **O**rdinary **D**ifferential **E**quations

PCA **P**rincipal **C**omponent **A**nalysis

PDE **P**artial **D**ifferential **E**quations

PEMS **P**ortable **E**mission **M**easurement **S**ystems

PIV **P**article **I**mage **V**elocimetry

PM **P**articulate **M**atter

POCS **P**eriodic **O**pen **C**ellular **S**ubstrates

RDE **R**eal **D**riving **E**missions

ROM **R**educed **O**rder **M**odel

SCM **S**ingle **C**hannel **M**odel

SCR **S**elective **C**atalytic **R**eduction

SDG **S**ustainable **D**evelopment **G**oals

SIMPLE **S**emi **I**mplicit **P**ressure **L**inked **E**quations

SST **S**hear **S**tress **T**ransport

TWC **T**hree **W**ay **C**atalytic Converter

UDF **U**ser **D**efined **F**unction

UI **U**niformity **I**ndex

URANS **U**nsteady **R**eynolds **A**veraged **N**avier- **S**tokes

UV **U**nit **V**ariance

WLS **W**eighted **L**east **S**quares

Chemical Species

C_3H_6 Propylene

CH_4 Methane

CO_2 Carbon dioxide

CO Carbon monoxide

H_2 Hydrogen

N_2O Nitrous oxide

N_2 Nitrogen

NO_2 Nitrogen dioxide

NO_x Nitrogen oxides

NO Nitric oxide

O_2 Oxygen

SO_x	Sulphur oxides

Greek Letters

α	permeability of fluid in porous media model
β	Closure constant
$\beta*$	Constant used in blending function in DES
β^*	Closure constant
χ_i	Species conversion
$\Delta H_{r,j}$	Heat of Reaction
Δ	Grid dimension in DES
δ_{ij}	Kronecker delta
$_t$	Total energy
$_i$	Component of gravity in the direction x_i
γ	Ratio of β and β^*
γ_a	Uniformity index for flow or temperature
$\hat{\omega}$	Weights applied to the predictor X
κ	Turbulent kinetic energy
λ	Thermal conductivity of fluid
μ	Molecular viscosity
μ_t	Turbulent viscosity
∇	Gradient operator
ν	Kinematic viscosity
ν_t	Turbulent kinematic viscosity
ν_{ij}	Stoichiometric coefficient
ω	Specific dissipation rate
$\overrightarrow{v}$	phase velocity in porous media
Φ	Dissipation function
ϕ	Constant in k-ω model
ϕ_1	Inner constant 1
ϕ_2	Inner constant 2
ϕ_a	Area weighted average of flow variable
ϕ_i	flow variable at face i
ρ	Fluid density
ρ_s	Density of solid
σ_ω	Turbulent Prandtl number for specific dissipation rate ω

σ_k Turbulent Prandtl number for turbulent kinetic energy k

$\sigma_{\omega 2}$ Closure constant

τ_{ij} Reynolds stress tensor

ε Error in the regression X

ε Porosity of the catalyst

ε Turbulent dissipation rate

English Symbols

u_i', u_j' Fluctuating velocity in tensor notation

$\bar{P}$ Mean pressure

$\bar{q}_i$ Mean heat flux

$\bar{T}$ mean temperature

$\bar{u}_i$, $\bar{u}_i$ Mean velocity in tensor notation

$\bar{J}_i$ Mean species flux due to diffusion

$\bar{Y}$ Mean species mass fraction

$\dot{S}_i$ Source term in energy equation

$\hat{Y}$ Predicted variable

Ω Vorticity magnitude

A Arrhenius frequency factor

A Number of principal components in PCA

A_i Face area

C_p Specific heat capacity of fluid

C_{DES} Coefficient used in blending function in DES

$C_{i,n}$ Concentration of species i in the $n^{th} tank$

C_{ij} Coefficient of inertial resistance of porous media

C_{p_g} Specific heat capacity of gas

C_{p_s} Specific heat capacity of solid

d Distance from the field point to the nearest wall

D_k Mass diffusivity of species

D_{ij} Coefficient of viscous resistance of porous media

E Residual matrix in PCA

E_A Activation energy

F_1 Damping function

F_2 Damping function

F_{DES} Blending function in DES

G	Inhibition factor(s) in DOC kinetics
I	Turbulent intensity
K	Number of variables in PCA
k_1	Rate constant of CO oxidation reaction
k_2	Rate constant of C_3H_6 oxidation reaction
k_3	Rate constant of NO oxidation reaction
K_i	Adsorption rate constants in DOC kinetics
K_{EQ}	Equilibrium constant in NO oxidation reaction in DOC kinetics
N	Number of observations in PCA
P	Loadings matrix in PCA
P	Production limiter
q	Volumetric flowrate
R	Source term for reaction rate
R_k	Net production of species by chemical reaction
R_{gas}	Universal gas constant
S	Specific area of a catalyst
S_i	Source term in RANS momentum equation
S_{ij}	Mean strain rate tensor
T	Scores matrix in PCA
t	time
T'	Fluctuating temperature
u	Instantaneous velocity
v	Residence time in a reactor
X	Data set in MVDA
X_i	Mole fraction of species i in DOC kinetics
x_j	Position vector in tensor notation
Y_k	Mass fraction of species
z	Axial flow direction

1 Introduction

This chapter briefly reviews emissions from automobiles, the need for 'aftertreatment', and the operational characteristics of exhaust aftertreatment systems (EATS). The objectives and contents of the thesis are presented in this chapter.

1.1 Background

The global surface temperature has increased by approximately 1.1 ° C above pre-industrial levels (1850-1900) during the last decade, with a warming trend observed to be higher over land (1.50°C) compared to the ocean (approximately $\sim 0.88°C$) in the last decade [1]. This increase in surface temperature is predominantly attributed to human anthropogenic activities, particularly the release of green house gases (GHG) such as carbon dioxide (CO_2), methane (CH_4), nitrous oxide (N_2O). A 54 % increase in GHG emissions equivalent to 21 Gt CO_2 was seen in 2019 as compared to the 1990 levels, and this trend is expected to continue further. The primary contributor to this increase was the CO_2 emissions from the combustion of fossil fuels and industrial processes. In the same year, 79 % of the GHG emissions originated from energy, industry, transport and building sectors combined, with the remaining 21 % coming from agriculture, forestry and other land use changes [1].

The year 2023 has been a very warm year breaching the 1.5 ° C mark and ocean temperatures have also reached record highs [2]. Global warming has triggered widespread and rapid changes in the atmosphere, oceans, and biosphere, resulting in adverse impacts on global weather patterns and climate extremes. Climate change has warmed the atmosphere, ocean, and land, contributing to rising sea levels and an increased frequency of extreme events such as heatwaves, heavy precipitation, droughts, and tropical cyclones [1]. These changes have caused substantial damage and irreversible losses to ecosystems, reduced food and water security, and hindered efforts to achieve sustainable development goals (SDGs). Additionally, the rise in extreme heat events has led to human mortality and morbidity, as well as the spread of climate-related diseases.

1.2 Emissions from automobiles and their effects

Internal combustion engines (ICE) have been popular until recent times due to their compact and robust nature, as well as the range and applicability they offer. Despite their many advantages, the emissions from ICEs are a cause of serious concern. The use of fossil hydrocarbon fuels in automobiles releases gases like carbon dioxide (CO_2), carbon monoxide(CO), unburnt hydrocarbons HC, particulate matter (PM) and oxides of nitrogen (NO_x). CO and HC are formed due to incomplete combustion of the fuel and imperfect mixing within the cylinder, whereas NO_x is formed due to the reaction between oxygen(O_2) and nitrogen(N_2) at high temperatures [3], consisting of nitric oxide (NO), nitrogen dioxide (NO_2), and small amounts of nitrous oxide (N_2O), and other species containing nitrogen and oxygen. These emissions are harmful to human life and

environment. They are linked to several short- and long-term health effects, including chronic obstructive pulmonary disease (COPD), cancer, wheezing, asthma, coughing, allergic reactions, and cardiovascular diseases. Additionally, they impact the ecosystem by affecting ambient air quality and influencing climate change [4].

1.3 Legislations

The California Air Resources Board (CARB) was set up in 1966 in California, pioneering emissions standards and catalytic converter development. Other states and countries subsequently adopted similar emission control legislation [5]. Setting up of CARB was a result of severe air pollution and smog in the 1940s. Initially, the source of the smog was attributed to gases from a butadiene plant. However, even after shutting down the plant, the smog persisted. It was later discovered that automobile emissions were the primary contributors to smog, leading to the formation of CARB.

The Euro emission standards, established by the European Union (EU), have undergone significant evolution from Euro 1 to Euro 6 [6], aiming to reduce harmful pollutants emitted by vehicles. Euro 1, introduced in 1992, mainly targeted carbon monoxide (CO) and hydrocarbon (HC) emissions. Subsequent standards, such as Euro 2 and Euro 3, incorporated stricter limits on nitrogen oxides (NO_x) and particulate matter (PM) emissions, reflecting growing concerns over air quality and public health. Euro 4 introduced emission limits for PM for light duty diesel vehicles, but the same was introduced in Euro 5 for light duty gasoline cars. Thus, in Euro 5b, comprehensive emission standards covering PM measurement, PN limits for diesel vehicles and low temperature emission testing for flex fuels and bio fuels were specified [7]. Euro 6, the most stringent standard to date, implemented tighter limits on NO_x and PM emissions for both gasoline and diesel vehicles, requiring advanced emission control technologies. Additionally, Euro 6 introduced on-board diagnostics (OBD) systems to monitor vehicle emissions in real-time. Both steady-state testing and transient testing are employed to assess vehicle compliance with Euro standards [7]. Steady-state testing involves running the vehicle under specific conditions to measure emissions, while transient testing simulates real-world driving scenarios to evaluate emissions during dynamic driving conditions, ensuring that vehicles meet emission standards under various operating conditions. These testing methods aim at better air quality and ensure that vehicles adhere to Euro standards. Similar norms exist for heavy-duty vehicles too; the difference between the light-duty standards and the heavy-duty standards is that the former is expressed as grams per kilometer run by the vehicle, whereas the latter is expressed as grams per kilowatt-hour [8]. The emission norms are specified in Roman numerals, such as Euro VI. In the forthcoming Euro 7 legislation, other types of emissions like non exhaust emissions (NEE) like particles from brake wear and tyres and gaseous emissions like nitrous oxide(N_2O), will also be regulated [9]. Both heavy duty and light duty vehicles will be included in the same legislation [9].

1.4 Composition of engine exhausts

The combustion of hydrocarbon based fuels or other fuel (H_2) with air in the Internal Combustion Engines (ICE) can be complete or incomplete. When hydrocarbon fuels are used, CO is the product of incomplete combustion, whereas CO_2 is formed under complete combustion conditions. The large fuel molecule also produces small but significant amounts of smaller hydrocarbons and PM. The composition of typical diesel engine exhaust and gasoline engine exhaust is given in Table 1.1 [10]. Fuels may have trace amounts of sulphur that produce sulphur oxides (SO_x) in the exhaust. The emissions also depend on the air-fuel ratio. The engine-out emissions require to be converted to CO_2 and water. Oxides of nitrogen that are formed in the combustion process have to be reduced to N_2. To achieve these products, catalytic converters are used [11]. Other possible options to reduce emissions are by modification of the engine design, use of exhaust gas recirculation (EGR) and use of alternate fuels and lubricating oils [12].

Table 1.1: Emissions from Diesel and Petrol Engines [10].

Mode	Range of Component		Units
	Diesel	petrol	
CO_2	7	10	%
CO	$10-15$	0.5	%
H_2O	$1.4-7$	10	%
CO	$300-1200$	5000	ppm
NO_x	$350-1000$	900	ppm
HC	$50-330$	350	ppm
H_2	$100-400$	1700	ppm
SO_x	$10-100$		ppm
PM	65		mg/m^3
N_2	Remaining	Remaining	%

1.5 Driving conditions

A vehicle can be driven under carefully controlled laboratory environment, for example, on a chassis dynamometer, or on-road. The emissions are then measured using portable emission measurement systems (PEMS) [13]. Three driving conditions are important from an emissions point of view. The first of these is coldstart driving, which occurs when the vehicle is started from rest. During coldstart, emissions are highest, as the catalyst is yet to light-off. The plot of species conversion as a function of temperature is termed the light-off curve. The engine exhaust warms up the EATS during operation; the time required depends on the thermal inertia. The second, real driving emissions (RDE) cover a wide variety of driving conditions and measuring the associated emissions using

PEMS. This procedure depends on the driving cycle adopted and is carried out to bring down the gap between the third category, 'laboratory condition emissions' and actual on-road driving condition emissions. Under Euro VI (d), the vehicle must comply with the emission legislation under cold start and RDE [7].

1.6 Exhaust aftertreatment systems

To comply with the legislation norms, emissions from the engine should be treated. This is achieved through catalytic reactions, as the energy barrier for a catalyzed reaction is much smaller than that of its uncatalyzed counterpart. One or more catalytic devices are used to treat engine-out emissions, often referred to as the exhaust treatment system. To suit the nature of diesel exhaust, which is rich in NO_x and PM, the aftertreatment system consists of one or more of the following in series: Diesel Oxidation Catalyst (DOC), Diesel Particulate Filter (DPF), Selective Catalytic Reduction Unit (SCR), and Ammonia Slip Catalyst (ASC). The sequence of exhaust aftertreatment systems for a petrol engine would be either a Three-Way Catalytic converter (TWC), Gasoline Particulate Filter (GPF), oxidation catalyst and NOx adsorber catalysts [14].

The transport processes that occur in catalytic converters are very complex and span different timescales [15]. Various measurements are essential for understanding and optimizing their performance, including velocity, temperature, and species concentrations. These measurements provide valuable insight into the flow dynamics, heat transfer, and chemical reactions that occur within the converter. However, obtaining measurements under transient conditions presents challenges due to limitations in instrument sensitivity and the speed at which these measurements can be taken relative to the transient timescale of the system.

Modeling allows for the exploration of a wide range of scenarios that may be challenging or impractical to investigate experimentally, thereby facilitating the optimization of catalytic converter design and operation. Furthermore, simulations can aid in predicting and understanding the impact of transient phenomena such as flow maldistribution and fluctuations, which are crucial for enhancing converter efficiency and meeting stringent emission regulations. Depending on the complexity and dimensions considered in modeling, the popular models are 1D models and 3D-CFD models.

1D models are widely used for simulating catalytic converters due to their simplicity, but accuracy diminishes in systems with flow maldistribution. Conversely, 3D computational fluid dynamics (CFD) simulations offer a more detailed representation of flow dynamics, including maldistribution effects, yet they come with significant computational costs. This thesis aims to bridge this gap by developing reduced-order models that balances computational efficiency with accuracy, thereby enabling more realistic simulations of catalytic converter performance under transient conditions, that can be used for design and control.

1.7 Objectives of the thesis

The objectives of this work are:

- To perform non-reactive simulations in order to quantify flow maldistribution in terms of uniformity index.
- To evaluate the effect of spatio-temporal fluctuations at the catalyst inlet on the time-averaged conversion at the catalyst outlet through reactive simulations.
- To develop a multi channel model by combining CFD solution and multi variate data analysis (MVDA) methods and compare its performance over full 3D solution and 1D solutions.
- To examine whether it is possible to predict species conversion accurately in systems with flow maldistribution, under steady state and under transient conditions, using steady state reactive 3D simulations at a lower computational effort.

1.8 Organization of the thesis

This thesis is organized as follows: firstly, a catalytic converter is introduced, and subsequently, several important transport phenomena and the operation of a catalytic converter are reviewed. This follows the discussion of the necessary theory to understand flow maldistribution and the factors that influence it, as well as the literature available for understanding it. An overview of modeling aspects of a catalytic converter is then presented, including 1D and 3D-CFD models, as well as chemometric modeling. The contents of the included papers are then summarized in the Chapter 4. Chapter 5 presents the conclusions and future prospects of the work. Chapter 6 discusses the contribution of this thesis to reduced order modeling of catalytic converters. Annexure gives details of the experimental details.

2 Background

The theoretical aspects of catalytic converter and flow maldistribution are presented in this chapter.

2.1 Working of catalytic converter

The goal of an aftertreatment system is to convert components from the engine-out gases to less harmful ones. The catalytic converter is a honeycomb monolith, as shown in Figure 2.1. Monoliths are produced from porous materials such as cordierite, and have numerous parallel channels. The walls of the channels are "washcoated" with precious metals dispersed on the highly porous substrate. The washcoat offers a large active surface for the catalytic reactions. The thickness of the washcoat varies from 10 μm to 150 μm [14]. The monolith is usually held in a metallic cage that serves to protect it from fracture.

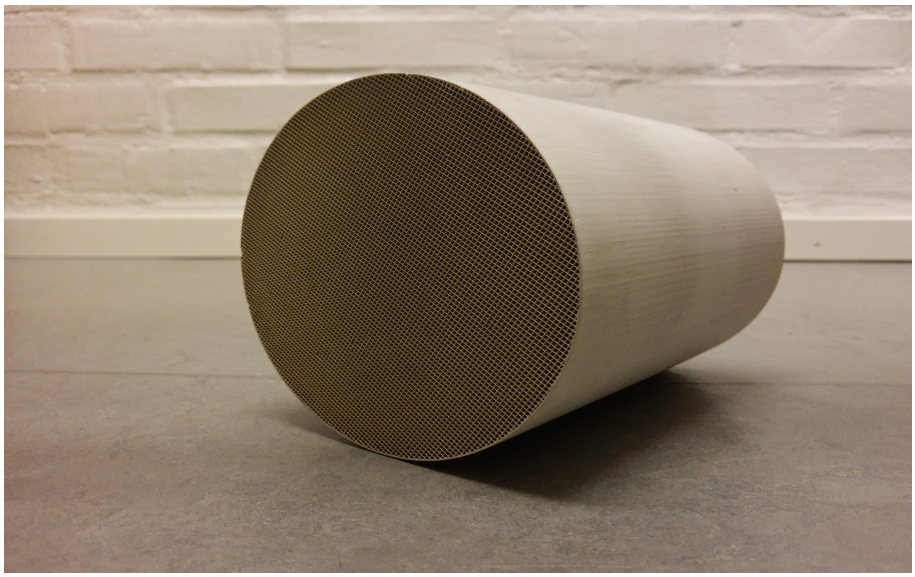

Figure 2.1: *Commercial catalytic converter (diameter 12 cm and 16cm long)*

The gases from engine travel through the catalytic converter.The cross section of catalytic converters are larger than the connecting exhaust pipe, cones are provided with smooth flow. The entry section has cones leading to the catalytic section. The hydraulic diameters are very small, and hence the flow of the engine-out gases in these channels is laminar and experiences small pressure drops. As they traverse the channels, they come into contact with the catalytic walls, where catalytic reactions occur. The advantages of using the monolith is multifold. Firstly, it offers a large surface-volume ratio. Secondly,

the pressure drop experienced by the gas flow is small [16].

Monoliths are manufactured in various cross sections, viz., circular, square, hexagonal, etc. They also have different sizes. Cells per square inch (CPSI) is a measure of the cell density or the number of channels in the monolith. Cordierite, metal foams, alloys are some of the materials of support for the monolith. The vibrations from the engine, thermal gradients and flow surge affect the ceramic substrated monoliths.

2.2 Transport processes in a catalytic converter

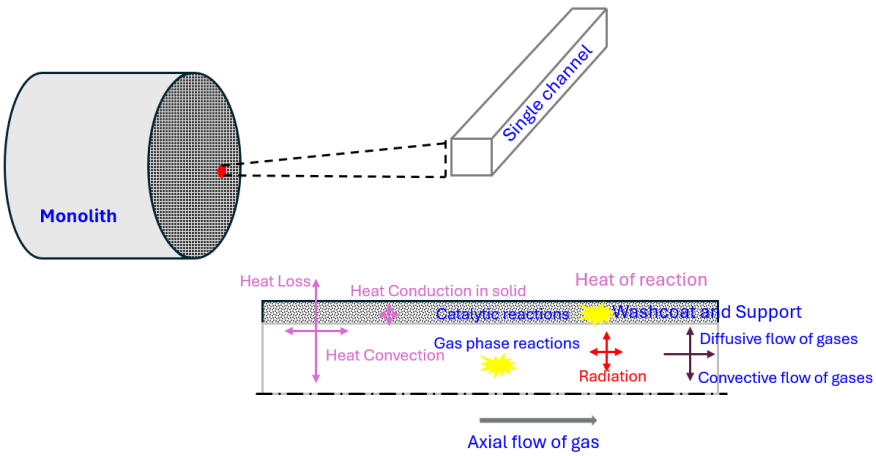

Figure 2.2: *Transport Processes in a catalytic converter.*

Figure 2.2 shows the different transport processes that occur in a catalytic converter. The transport processes that happen inside the monolithic catalytic converter are complex and they span different timescales [15]. The channels provide an open structure facilitating the flow of gases through the channel. Engine-out gases that have to be treated are fed to the catalytic converter. These gases transfer momentum, mass and energy in the channels. Reactants diffuse towards the inner channel wall, coated with a porous structure (washcoat) supporting catalytic material, where surface reactions occur. Gas phase reactions occur in bulk. The species move axially by convection and radially by diffusion. The radial movement of species towards the wall allow the species to adsorb onto the active catalytic sites, for surface reactions. Radicals, intermediates can also react on the surface or in the gas phase. The products desorb and diffuse back to the bulk flow. Temperature field inside the monolith is influenced by the heatS of reactions of the homogeneous and heterogeneous chemical reactions[14]. Temporal and spatial variation of the gases at the inlet can affect the temperature field across the monolith and channel-to-channel variation.

The performance of a catalytic converter is a function of temperature. The range of temperatures upto which the performance (conversion) of the catalyst is maximum is termed the catalyst window. The conversion of the reactants depends on the size of the catalyst, active metal loading and the residence time of reactants in the catalyst [11]. This residence time is expressed as gas hourly space velocity (GHSV), which has units of inverse of time (h^{-1}). GHSV is defined as the ratio of volumetric flow at standard conditions to the volume of the catalyst [17]. Another important characteristic of the monolith is the *light-off* temperature. This is the temperature at which at least 50 % of the reactants are converted.

Energy is transferred within the monolith and to the ambient. Heat is convected along the axial direction by the gas flow through the monolithic channels. The solid walls are heated by the hot gases and by the heat generated from the exothermic catalytic reaction, which in turn exchange heat with the ambient and flowing gases. Catalytic converters are usually insulated with multiple layers of insulation. Radiative heat transfer becomes significant after light-off temperatures. Conduction is the energy transport in the solid region, whereas convection is the transport in the fluid phase. Radiation is significant at high temperatures.

Various physical phenomena affect the performance of catalytic converters, including temperature variations, fluctuations in the composition and pressure of the combustion gas, ageing and degradation of the catalyst, poisoning by contaminants, physical damage, and vibrations. These factors can affect catalytic reactions, flow dynamics, and overall efficiency. This thesis will comprehensively address the challenges posed by flow maldistribution, fluctuations, and pulsations in engine exhaust. Additionally, it will focus on developing a reduced-order model (ROM) that accurately captures the complex interactions within the catalytic converter, considering the multitude of physical phenomena involved.

2.3 Flow distribution in catalytic converters

The flow to the catalytic converter from the engine is usually transient and has fluctuations. As a result of space constraints in the vehicle design, complex flow patterns are introduced in the manifold and at the catalytic converter inlet. These factors contribute to non-uniform flow, resulting in flow distribution at the inlet of the catalytic converter.

2.3.1 Effects of flow maldistribution

The flow maldistribution is primarily occurs exhaust manifolds in the engine leading to the inlet of the EATS. Flow maldistribution is important to be given attention due to the following reasons [18]:

(i) Flow maldistributions leads to differences in flowrates within the catalytic converter. 1D-models have limited accuracy in representing flow maldistribution. 1D-models assume all channels in the catalytic converters behave exactly similar in terms of conversion and temperature. This assumption does not hold when there are

differences in flow or when there is flow maldistribution. Differences in flowrates introduces variable residence times in the channels. This manifests as varying conversion in the channel. Analysis of flow maldistribution are explained in Paper I and the definitions of uniformity index for different flow variables such as velocity and temperature are discussed.

(ii) Certain regions of the catalyst experience lower flowrates, leading to non-uniform utilization of catalyst.

(iii) Flow maldistribution also leads to temperature distribution in the monolith. Some channels experience higher temperatures. The temperature distribution also affects the light-off characteristics and conversion. It also affects attrition and ageing of catalysts.

2.3.2 Factors affecting flow maldistribution

The activity of catalytic converters is directly linked to the temperature. The catalytic converter attains its rated performance above its light-off temperature. This is achieved by hot exhaust gases from the engine heating the catalytic converter. The two most common placements for catalytic converters involve positioning them either near the engine-out exhaust exit (referred to as close-coupled catalysts) or further downstream (known as under-body catalytic converters). The placement of the catalytic converters significantly influences the flow distribution at their inlet. Inlet and exit cones in catalytic converters serve as mixing regions, with the cone angle designed to minimize flow separation, a constraint driven by automotive design compactness (Figure 2.3). Holmgren et al [19] demonstrated the impact of inlet cone design on flow uniformity. The inlet fluctuations also affect the uniformity of flow to the monolith, altering the mass flow to the catalyst. CFD simulations are also used in optimization of cone angles. Nonuniform rational B-splines (NURBSs) have used to design and optimze the cone angles and improve flow uniformity in diesel particulate filters, gasoline particulate filters [20, 21]. Experiments and simulations are performed to design optimal cone connection shapes [21, 22] In a classical monolith, there is no mass transfer between channels. Once flow maldistribution sets in, improving distribution is challenging. A way to promote flow between channels is by using periodic open cellular substrates (POCS) and hence improve flow distribution [23].

Figure 2.3: *Bends in a catalytic converter.*

2.4 Flow uniformity index

Flow uniformity index (UI) is used to quantify the nature of distribution of flow in a catalytic converter. The UI is a dimensionless scalar, and is an averaged ratio that is calculated at any plane in a catalytic converter. Exit plane of the monolith and exit of the EATS are usually chosen to assess the uniformity of flow in terms of UI.

UI gives the deviation of a flow variable from the mean value of the flow variable. The definition UI is given by the formula [24]:

$$\gamma_a = 1 - \frac{1}{2}\left(\frac{\sum_{i=1}^{n} |\ \phi_i - \overline{\phi_a}\ | A_i}{\overline{\phi_a} \sum_{i=1}^{n} A_i}\right) \tag{2.1}$$

where

$$\overline{\phi_a} = \frac{\sum_{i=1}^{n} \phi_i A_i}{\sum_{i=1}^{n} A_i} \tag{2.2}$$

where ϕ_i is the flow variable (velocity, temperature) in the face i, $\overline{\phi_a}$ is the area-weighted average of the flow variable, and A_i is the area of face i.

The range of UI values ranges from 0 to 1. The flow is considered to be very uniform for values of UI closer to 1. A 20% relative deviation in the flow from the mean (term within the brackets), will give a flow uniformity index of 0.9. UI is affected by the angle of the inlet cones of the monolith, pulsations or fluctuations in the inlet velocity, inlet conditions such as the velocity, temperature and concentration. It is noteworthy that a difference of flow variable from the average value is used in the definition. The choice of the definition of flow variable influences the value of UI. Several definitions are used by researchers to express the UI [19, 25, 26]. Since the simulations in this work are carried out in ANSYS Fluent, the definition followed in ANSYS Fluent is used in this work [24].

UI can be estimated by experimental techniques or by simulation. Measured value of the flow variable is required, techniques like hot wire anemometry can provide the velocity at a point. Thermocouples can be used to record temperature measurement. The limitation of measurements is that the probe for measurement should not interfere with the flow path or flow field. Non-destructive techniques like Particle Image Velocimetry (PIV) or Laser Induced Fluorescence (LIF) can come handy in getting the distribution at the inlet and/or exit in optically transparent rigs. UI can also be obtained through simulations. To this end, solutions to the equations of momentum, energy, and species

are required. The advantage of CFD is that the UI can be calculated at any plane of interest in the monolith.

2.5 Modeling of catalytic converters

2.5.1 Single channel model (SCM)

1D models are the simplest mathematical description of a catalytic converter. One such model is called the single channel model (SCM). Here, it is implicitly assumed that the flow is evenly distributed among all channels and that there is no exchange of heat, mass, or momentum between the channels. Under conditions where the flow distribution is uniform and the heat exchange is negligible, each channel will exhibit similar behavior in terms of reactive transport processes. This means that every channel experiences identical flowrate, temperature, and concentration of species at the inlet. The species conversion is then a function of residence time and the temperature and kinetics. Thus, one channel is considered representative, and modeling this channel alone is sufficient to predict the performance of the entire monolith [27]. The washcoat and channels operate on different timescales and length scales due to variations in aspect ratio and nonuniform thickness of the washcoat. To represent these transport processes that range such varying timescales requires fine resolution. Energy and species transport are described by partial differential equations (PDE) with specified inlet velocity and concentration of species.

2.5.2 3D-CFD models

3D-CFD modeling of catalytic converters offers a more detailed representation of flow dynamics and chemical reactions compared to 1D-SCM. Advantages include the ability to capture complex geometries and flow phenomena, such as flow maldistribution, coldstart and RDE, which are crucial for accurate predictions of converter performance. Unlike the 1D-SCM, radial heat transfer is accounted, which becomes important to be included in realistic geometries with flow maldistribution. Additionally, 3D-CFD models can provide insights into temperature and species concentration distributions throughout the converter. However, 3D-CFD simulations are computationally expensive and require significant computational resources and time, compared to their 1D counter parts

2.6 Existing literature and knowledge gap

Various modeling approaches have been employed to understand the transport processes in catalytic converters and to predict the concentration of gases at the tail pipe. The tailpipe gas concentration holds significant importance for two primary reasons: first, to comply with emission regulations, and second, to enhance overall performance. Frequently, a catalytic converter is succeeded by an additional emission control device, such as a Selective Catalytic Reduction (SCR) system following a Diesel Oxidation Catalyst (DOC). The DOC plays a crucial role in oxidizing NO to NO_2, thereby improving the efficiency of the SCR system [28]. While measuring tailpipe gas concentrations is feasible, transient

operations present challenges to accurate measurements. Consequently, there is a growing necessity to predict tailpipe concentrations through numerical simulations, providing a dependable method for predicting emissions across diverse operating conditions.

It is crucial for such simulations to incorporate a comprehensive mathematical model that accurately represents the complex coupled physico-chemical processes in a catalytic converter. To be effective, these simulations must meticulously consider the physical design attributes and operating conditions typical of real-world systems. Mathematical models range from simplistic one-dimensional (1D) representations to more complex 3D-CFD simulations. Each modeling approach offers unique advantages and limitations, influencing its applicability for predictive modeling, optimization and control purposes. The classification of modeling for these devices is based on assumptions regarding flow distribution and the interactions of heat and mass within them. Solutions for these models are obtained using 1D models and higher-dimensional models, each with their own set of assumptions.This section presents the various modeling approaches in the literature.

Further, kinetic rate expressions play a crucial role in modeling the chemical reactions occurring within catalytic converters. These expressions describe the rate at which reactants are transformed into products on the catalyst surface. Two main types of rate expression are commonly used: global rate expressions and microkinetic rate expressions. Global rate expressions provide a simplified representation of the overall reaction kinetics, typically assuming a single-step reaction mechanism with an empirically determined rate constant. In contrast, microkinetic rate expressions offer a more detailed and mechanistic description of the individual elementary steps involved in the reaction pathway. These expressions account for factors such as adsorption, desorption, and surface reaction energies, providing insights into the underlying molecular-level processes [29]. Understanding and accurately parameterizing these kinetic rate expressions are essential for developing predictive models of catalytic converter performance and optimizing catalyst design.

A distributed parameter 1D model of a catalytic converter is the heterogeneous model [14], where a single channel is modeled by solving the energy balance and species conservation equations. Taking C_{i_g}, T_g as the concentration of species i and the temperature of the gas phase and C_{i_s}, T_s as the concentration of species i and temperature of the solid phase, these two phases are connected by a film model using mass transfer and heat transfer coefficients. This results in a system of differential algebraic equations (DAE). Alternatively, the heterogeneous model can be simplified assuming that the concentration of the species i and the temperature are identical in the wall and in the gas phase. This requires an effectiveness factor to relate the inherent kinetics to the apparent kinetics. This is termed as the pseudo homogeneous model.

Earliest works with the reference of SCM can be attributed to the works by Young and Finlayson [30, 31] and Oh and Cavendish [32]. These works described 2D variations in temperature field and the solution to convection diffusion reaction (CDR) model respectively. Authors have used detailed kinetics and global kinetics to model reactions

in catalytic converters [33–36]. Further improvements with modeling of the monolith were attempted, *viz.,* effectiveness factor to include the species diffusion in the washcoat [37, 38], oxygen storage in 1D model [39], prediction of light-off curves using detailed kinetics [33], or the use of 1D heterogeneous model with global kinetics [34], capturing mass transfer effects on a 1+1D model [40–43], with internal mass transfer resistances were incorporated in the SCM model by using effectiveness factor [37, 44–46], a model that captures the washcoat geometry effects [47], the effects of upstream turbulence on the heat and mass transfer effects in a single channel monolith [48]. To include heat and mass transfer effects, correlations of Nusselt number and Sherwood number have been used to relate the transport processes with the monolith wall and the interior [39, 49].

Weltens et al showed that 3D simulations are necessary to capture performance characteristics in complex geometries with bends [50]. Mei et al. conducted a comparison between experiments and simulations of the catalytic combustion of the methane-air mixture in a monolithic reactor, revealing that the 3D model provided a closer match to the experimental data compared to the single-channel model [51]. Similar findings were reported by Kumar and Mazumder [52]. Some authors have modelled all channels of the catalytic converter [53–55], and in some cases, an axisymmetric assumption was utilized to reduce the computational load. A porous media approximation for the catalyst can help reduce computational complexity [56], the pulsating inlet conditions of EATS were simulated using 3D CFD with the assumption of porous media [57]. A multizone permeability approach is also used to describe the catalytic part of the monolith [58].

Several works have reported the steady state uniformity index analysis in catalytic converters using CFD simulations [19, 55, 56]. These works either resolvemonolith channels individually by modeling a limited number of channels [55] or by following a porous media approach to describe the monolith [56] or by describing the pressure drop relation in a more detailed manner [59]. Some studies have attempted transient simulation [59–61]. Other studies describe the turbulence generation and decay inside the catalytic converters [62, 63].

In scenarios characterized by flow maldistribution, the inlet of the catalyst experiences a non-uniform flow field, thereby limiting the applicability of Single Channel Models (SCM). In such cases, 3D Computational Fluid Dynamics (CFD) simulations offer a viable alternative. However, for large geometries, conducting transient reactive simulations through 3D-CFD entails significant computational effort. This leads to prolonged solution times, consequently constraining their utility in design and control applications. Phenomena like coldstart, RDE, geometries with bends pose challenges in obtaining simplified reactor models. A lower-dimensional model, such as a "few 1D" model, would be very desirable, as it allows for the utilization of multiple inlet locations with varying velocities, temperatures, and species concentrations by combining their contributions. This approach can yield results with accuracy comparable to that of CFD while maintaining simulation times comparable to those of an SCM. Alternatively, a parameter can be identified that can correlate the actual channel/catalytic converter with a fictitious reactor. Multichannel models have been referred in literature like the works of Chakravarthy et al

[59] and Aslanjan et al [60]. In the former, channels were lumped by employing coarse mesh grid, and in the latter specific channel locations were chosen to have position-varying inlet temperature specification. In these two approaches, efforts have been made to specify position dependent properties, but they do not offer a generalized methodology for determining the number of such positions to be specified.

Methods of multivariate data analysis (MVDA) have been previously employed in computationally demanding processes such as combustion kinetics [64, 65] and estimation of parameters of heterogeneous catalytic reactions [66]. However, such a method has not been applied on EATS, or in developing a multi-channel model for a catalytic converter. This study proposes to develop multi-channel model and "few 1D" channels by combining the CFD solution and applying chemometric techniques on the CFD solutions. "Few 1D channels" with inlet parameters specified at multiple inlet locations can be referred to as multi-channel models. The next chapter gives an account of all the modeling procedures used in this thesis, followed by the simulation conditions.

3 Modeling

Exhaust emissions are converted to less harmful products using catalytic converters. The conversion efficiency of a species in a catalytic converter is influenced by temperature and residence time. Coldstart emissions contribute significantly to the overall accumulated emissions from vehicles. Therefore, models must be robust to be able predict generic as well as challenging conditions like pulsations, flow maldistribution and coldstart. To this end, 1D and 3D simulations are used to obtain the flow field solution.

While 1D simulations are robust and computationally effective, phenomena like flow maldistribution, coldstart and RDE limit their accuracy. Conversely, 3D simulations perform better in depicting the multiphysics in catalytic converters, however, computational effort poses a constraint. The primary goal of this thesis is to derive a multi-channel model (MCM) for a catalytic converter and this is achieved predominantly through numerical simulations.

The chapter describes the model equations that characterize the flow field in a catalytic converter. The flow field is characterized by velocity components, temperature and species concentrations. This chapter discusses the model equations that are solved in the numerical simulations.

The following assumptions are made in the model development:

(i) Non reactive simulations utilize air as the working fluid.

(ii) Reactive simulations utilize a gas mixture of the exhaust gas consisting of CO, CO_2, O_2, C_3H_6, NO, NO_2, H_2, H_2O and N_2 as the fluid.

(iii) Gas phase behavior is assumed to be ideal and Newtonian under the operating conditions.

(iv) The monolith is assumed cylindrical with circular cross section.

(v) The fluid flow is incompressible.

(vi) Radiation effects are deemed insignificant given the operating conditions.

(vii) Laminar flow is enforced in the catalyst section.

(viii) Gravity effects are not included in the model.

3.1 Flow field

In the catalytic converter, the fluid is comprised of a gas mixture, and the continuum assumption is adopted in this study. The flow field is characterized by velocity components, temperature, and species concentrations. The flow field fulfills the laws of conservation of

mass, momentum, and energy within the flow field. These fundamental principles result in a set of differential equations governing the balance of these variables within a control volume. Specifically, the conservation of mass leads to the continuity equation, while the momentum balance equation stems from Newton's second law of motion. In the case of Newtonian fluids, this equation is commonly referred to as the Navier-Stokes equation.

The law of conservation of energy yields the energy equation, while the mass balance on the species gives species continuity equation. To obtain the values of the flow field at any plane, the solution of Navier-Stokes equation is to be sought for the components of velocity, the energy equation for temperature and species continuity equation for the species concentrations. These equation are collectively termed as equations of change, as they are cast in the differential form. Solution of these equations gives the spatial and temporal description of the flow field. The energy and species continuity equations may have source terms like heat loss or presence of a reaction term [67].

The equations of change are partial differential equations. They require appropriate initial and boundary conditions for the solution. The no-slip conditions are enforced on the wall, where the velocities are zero for a stationary wall. Other specifications may include Dirichlet or Neumann or mixed boundary conditions. The outlet can be specified as a pressure outlet with zero gauge pressure. Zero gradients are specified for other variables.

3.1.1 Governing equations in differential form

The following are the equations of change for fluid flow [67] :

Equation of continuity
This states that mass cannot be created or destroyed, and is given by

$$\frac{\partial \rho}{\partial t} + \frac{\partial (\rho u_i)}{\partial x_i} = 0 \tag{3.1}$$

where t and x represent temporal and spatial coordinates respectively, and ρ is the density of the fluid and u_i is the velocity of fluid in the coordinate direction x_i.

Equation of momentum
This states that the rate of change of momentum over time within the control volume is the net sum of external forces acting on the control volume minus the net rate of momentum out of the control volume. When this is applied for a Newtonian fluid, the resulting equations are termed as Navier-Stokes equations, and is given by:

$$\frac{\partial (\rho u_i)}{\partial t} + \frac{\partial (\rho u_i u_j)}{\partial x_j} = -\frac{\partial p}{\partial x_i} + \frac{\partial \tau_{ij}}{\partial x_j} + \rho g_i \tag{3.2}$$

Here, τ_{ij} is the stress tensor, p is the pressure and g_i is the component of gravity in the coordinate direction x_i.

Equation of energy
This states that energy cannot be created or destroyed but can be transformed from one form to another, and is given by :

$$\frac{\partial(\rho E_t)}{\partial t} + \frac{\partial(\rho u_i E_t + p)}{\partial x_i} = \frac{\partial}{\partial x_i}\left(k\frac{\partial T}{\partial x_i}\right) + \frac{\partial}{\partial x_i}\left(\tau_{ij}u_j\right) + \dot{S}_i \tag{3.3}$$

where, E is the total energy, T is the temperature of the fluid, $\dot{S}_i$ is the source term.

Equation of continuity for species

This equation is the conservation of mass of species:

$$\frac{\partial(\rho Y_k)}{\partial t} + \frac{\partial(\rho u_i Y_k)}{\partial x_i} = \frac{\partial}{\partial x_i}\left(D_k\frac{\partial Y_k}{\partial x_i}\right) + R_k \tag{3.4}$$

Here, Y_k is the mass fraction of the species, D_k is the mass diffusivity and R_k is the net production of the species by chemical reaction.

These equations are partial differential equations. Owing to their non-linear and coupled nature, analytical solutions are but, available for very simplified cases. For a realistic problem, solution methodology can be obtained numerically. Experimental observations can also provide solutions, more often, for a limited number of cases. The numerical solutions are usually termed as computational fluid dynamics (CFD) solutions. A number of software, commercial or open source are available for getting CFD solutions. The original differential equations are converted to algebraic equations by discretization process [68]. The solutions are usually obtained iterative algorithms. CFD simulations offer flexibility in exploring complex flow phenomena and scenarios that may be challenging to replicate in experimental setups, allowing for more in-depth investigation and analysis of fluid flow problems. The validation of these solutions can be done with experimental data and /or physical laws.

3.1.2 Steps in obtaining solution using CFD

The numerical simulations are performed using computational fluid dynamics (CFD) technique. In the CFD approach, the steps are as follows: defining the geometry of interest, discretizing into computational nodes / cells, discretizing the equations of change and the inital and boundary conditions. There are three different CFD approaches, depending on the methodology adopted by the solution. They are the finite difference method (FDM), finite volume approach [69] and the finite element method (FEM) [70]. In this work, finite volume approach is adopted and a commercial software ANSYS FLUENT is used for the CFD solutions. In this work, finite volume method (FVM) is the discretization method. FVM discretizes the computational domain into a finite number of control volumes. These control volumes, often polyhedral or Cartesian in shape, enclose portions of the domain where the governing equations are integrated. The method inherently

conserves mass, momentum, and energy within each control volume, making it well-suited for simulating physical processes governed by conservation laws. By applying appropriate boundary conditions and spatial discretization schemes, such as central differencing or upwind schemes, the governing equations are discretized and solved iteratively over the discretized domain. This iterative process allows for the accurate prediction of flow properties, including velocity, pressure, and temperature distributions, providing valuable insights into complex fluid flow phenomena.

3.1.3 Turbulence in fluid flows

Solution of the equations Eq. 3.1 to 3.4, as function of time using iterative procedure,provides the information of the flowfield. Truncation error arises due to the approximation methods used in the discretization [68]. To be able to get the solution of instantaneous variable $u = u(t)$, the discretization needs very fine resolution of the computational cells. The solution method is direct numerical simulation (DNS), the computational cost is prohibitively large. This computational cost exponentially increases as the cube of the Reynolds number[71]. To be able to reduce this overwhelmingly computational load, approximations are introduced and these are referred to as turbulence modeling.

In this work, the mean field solution of flow field is obtained by applying an approximation that is termed as Reynolds averaged Navier Stokes equations, as described in 3.2. A brief section on the validity of URANS is tested by doing detached eddy simulations (DES), this is explained in 3.9.

3.1.4 Unsteady Reynolds averaged Navier-Stokes equations

The instantaneous solution variable $u(t)$, is expressed as a sum of mean of the variable, $(\overline{u_i})$, and a fluctuating component that captures the time varying nature, (u_i'). This is called Reynolds decomposition. By applying Reynolds Averaging procedure,we focus only on the averaged components. The chosen time scale for averaging should be much larger than the frequency of fluctuations but smaller than the time period of the mean flow. This procedure leads to the emergence of a term called Reynolds Stresses. Turbulence models are then used to appropriately handle these stresses [72].

The time-averaged Navier Stokes equations obtained through Reynolds averaging procedure are referred to as Unsteady Reynolds averaged Navier-Stokes (URANS) equations. These equations allow us to obtain the flow field variables. Turbulence is modeled using appropriate turbulence models [72]. The URANS formulation reduces the computational load quite significantly. The limitations of a turbulence model are wall bounded flows, turbulent fluctuations and geometries of non-circular cross section [73].

3.1.5 Turbulence Modeling

In the laminar part of flow, the shear stress is proportional to the velocity gradient. Molecular viscosity serves as the proportionality constant. Similarly, we can assume that the Reynolds stresses have the same form as the laminar counterparts. The apparent turbulent shear stress is proportional to the mean strain. This is the Boussinesq hypothesis [72]. The proportionality constant in this case is the turbulent viscosity or eddy viscosity. Computing turbulent viscosity is done by a turbulence model, in terms of turbulent kinetic energy (κ) and turbulent dissipation rate (ε) or specific dissipation rate (ω). The turbulent viscosity can then be used to compute the Reynolds stresses [74].

In this work, shear stress transport SST $\kappa-\omega$ model is chosen to compute the turbulent viscosity. The advantages of SST $\kappa-\omega$ model are: it is suited to handle low Reynolds number flows, and, it can handle the viscous sub-layer and transition flows.

3.2 Governing equations for URANS

The equations of continuity, momentum, energy and species concentration in the RANS form are presented in this section.

3.2.1 Non-catalytic section

The equations that are solved are the continuity equation, momentum balance equation for the velocity components, the energy balance equation. The equations of continuity, momentum and energy are time-averaged by Reynolds Averaging procedure and are presented below in the differential form. The time-averaged variables are denoted with the overhead bars.

The equation of continuity in the time-averaged form is given below.

$$\frac{\partial \rho}{\partial t} + \frac{\partial (\rho \bar{u}_j)}{\partial x_j} = 0 \tag{3.5}$$

Here, x and t represent spatial and temporal coordinates respectively, the fluid density is given by ρ in (kg/m^3), and u_j is the velocity (m/s) in coordinate direction x_j .

The time-averaged momentum balance equation is

$$\rho \left(\underbrace{\frac{\partial \bar{u}_i}{\partial t}}_{\text{local acceleration}} + \underbrace{\bar{u_j} \frac{\partial \bar{u}_i}{\partial x_j}}_{\text{Convective acceleration}} \right) = \underbrace{-\frac{\partial \bar{p}}{\partial x_i}}_{\text{Pressure gradient}} + \underbrace{\frac{\partial \tau_{ij}}{\partial x_j}}_{\text{Gradient of Stress}} + \underbrace{S_i}_{Sourceterm} \tag{3.6}$$

where p is the pressure (Pa), S_i is a source term representing the presence of the monolith brick on the flow (kg/m·s), and τ_{ij} is the stress tensor:

$$\tau_{ij} = \underbrace{\left(\mu\frac{\partial \bar{u_i}}{\partial x_j} + \frac{\partial \bar{u_j}}{\partial x_i}\right)}_{\text{Laminar Shear Stress Contribution}} - \underbrace{\rho\overline{u_i' u_j'}}_{\text{Reynolds Stress (Turbulent Contribution)}} \tag{3.7}$$

μ is the dynamic viscosity of the fluid (Pa.s).

3.2.2 Turbulence modeling

The SST $\kappa - \omega$ model is used for turbulence closure, to estimate the Reynolds stresses. The Reynolds stresses are estimated via the turbulent viscosity. Two equations, one each for the turbulent kinetic energy k (m^2/s^2), and the specific dissipation rate ω (1/s) are needed to model turbulent viscosity [74]. The transport equation for k is

$$\frac{\partial(\rho\kappa)}{\partial t} + \frac{\partial(\rho\bar{u_j}\kappa)}{\partial x_j} = P - \beta^*\rho\omega\kappa + \frac{\partial}{\partial x_j}\left[(\mu + \sigma_\kappa\mu_t)\frac{\partial\kappa}{\partial x_j}\right] \tag{3.8}$$

where P is the production limiter, β^* is the closure constant used in the model, and σ_κ is the turbulent Prandtl number for the turbulent kinetic energy (κ) and μ_t is the turbulent viscosity. The transport equation for ω is

$$\begin{aligned}\frac{\partial(\rho\omega)}{\partial t} + \frac{\partial(\rho\bar{u_j}\omega)}{\partial x_j} = \frac{\gamma}{\nu_t}P - \beta\rho\omega^2 + \frac{\partial}{\partial x_j}\left[(\mu + \sigma_\omega\mu_t)\frac{\partial\omega}{\partial x_j}\right] + \\ 2(1 - F_1)\frac{\rho\sigma_{\omega 2}}{\omega}\frac{\partial\kappa}{\partial x_j}\frac{\partial\omega}{\partial x_j}\end{aligned} \tag{3.9}$$

where β is a closure constant, γ is the ratio of β and β^*, ν_t is the turbulent kinematic viscosity, σ_ω is the turbulent Prandtl number for ω, $\sigma_{\omega 2}$ is also a closure constant, and F_1 is a damping function.

More specifically,

$$\begin{aligned} P &= \tau_{ij}\frac{\partial\bar{u_j}}{\partial x_j} \\ \tau_{ij} &= \mu_t\left(2S_{ij} - \frac{2}{3}\frac{\partial\bar{u_\kappa}}{\partial x_\kappa}\delta_{ij}\right) - \frac{2}{3}\rho\kappa\delta_{ij} \\ S_{ij} &= \frac{1}{2}\left(\frac{\partial\bar{u_i}}{\partial x_j} + \frac{\partial\bar{u_j}}{\partial x_i}\right)\end{aligned} \tag{3.10}$$

The following formula is used to compute the turbulent viscosity:

$$\mu_t = \frac{\rho a_1 \kappa}{max(a_1\omega, \Omega F_2)} \tag{3.11}$$

The damping functions and other constants required to compute the turbulent viscosity are obtained as shown below:

$$\phi = F_1\phi_1 + (1 - F_1)\phi_2$$

ϕ_1 and ϕ_2 are the inner constants 1 and 2.

$$F_1 = tanh(arg_1^4)$$

$$arg_1 = min\left[max\left(\frac{\sqrt{\kappa}}{\beta * \omega d}, \frac{500\nu}{d^2\omega}\right), \frac{4\rho\sigma_{\omega 2}\kappa}{CD_{\kappa\omega}d^2}\right]$$

$$CD_{k\omega} = max\left(2\rho\sigma_{\omega 2}\frac{1}{\omega}\frac{\partial\kappa}{\partial x_j}\frac{\partial\omega}{\partial x_j}, 10^{-20}\right)$$

$$F_2 = tanh(arg_2^2)$$

$$arg_2 = max\left(2\frac{\sqrt{\kappa}}{\beta * \omega d}, \frac{500\nu}{d^2\omega}\right)$$

In the above expressions, d is the distance to the nearest wall from the field point. Ω is the vorticity magnitude and is given by

$$W_{ij} = \frac{1}{2}\left(\frac{\partial\bar{u_i}}{\partial x_j} - \frac{\partial\bar{u_j}}{\partial x_i}\right)$$

Default constants from ANSYS Fluent were used in the work. Additional description and details about the terms and functions in the SST $\kappa - \omega$ model are provided by Menter [74].

The time-averaged energy equation is

$$\rho C_p\left(\frac{\partial\bar{T}}{\partial t} + \bar{u_i}\frac{\partial\bar{T}}{\partial x_i}\right) = -\frac{\partial\overline{q}_i}{\partial x_i} + \bar{\Phi} \tag{3.12}$$

where the dissipation function $\bar{\Phi}$ is given by

$$\bar{\Phi} = \frac{\mu}{2}\left(\frac{\partial \bar{u_i}}{\partial x_j} + \frac{\partial u_i'}{\partial x_j} + \frac{\partial \bar{u_j}}{\partial x_i} + \frac{\partial u_j'}{\partial x_i}\right)^2$$

and

$$q_i = -\lambda\frac{\partial \bar{T}}{\partial x_i} + \rho C_p \overline{u_i' T'}.$$

The time-averaged species continuity equation that governs the spatio-temporal evolution of the reactant mass fraction $\bar{Y}$ is as follows:

$$\left(\frac{\partial \rho \bar{Y}}{\partial t} + \bar{u_i}\frac{\partial \rho \bar{Y}}{\partial x_i}\right) = -\frac{\partial \bar{J_i}}{\partial x_i} + R \tag{3.13}$$

The term $\bar{J_i}$ represents the species flux due to diffusion and R represents the source term due to chemical reaction.

The turbulent contributions to $\overline{q}_i$ and $\overline{J}_i$ are handled within the SST $k-\omega$ framework.

3.3 Flow field equations for the catalytic section

The catalytic section features a monolith structure characterized by its density of channels per square inch. External porosity is measure of the area (or volume) available for the fluid flow. The flow within the monolith predominantly exhibits laminar behavior. As the fluid transitions from the non-catalytic section to the catalytic section, it undergoes a shift from a turbulent to a laminar regime. In an actual honeycomb monolith, there is no mass transfer between the channels, this means that flow in every channel progresses in the axial direction and the radial flow is prohibited because of the presence of channel walls.

The monolith channels can be modeled individually to obtain the flow field in the monolith. This approach would be very computationally-intensive owing to the large number of channels. Another alternate approach is to use a lumped parameter approach. In this method, the monolith is approximated as a porous media. The porous media is approximated as momentum sink. The turbulence viscosity and turbulent production are set to zero.

ANSYS Fluent uses superficial velocity formulation [24]. The porous media is modeled by a source term in the momentum equations. The flow experiences pressure drop as it passes through the monolith. This pressure loss source term is a sum of two terms: viscous term and inertial term [24]. The inertial pressure drop is proportional to the square of velocity and the viscous term is proportional to the velocity.

$$S_i = -\left(\sum_{j=1}^{3} D_{ij}\mu v_j + \sum_{j=1}^{3} C_{ij}\frac{1}{2}\rho|v|v_j\right) \tag{3.14}$$

For the inertial term, the pressure drop is given by

$$\nabla P = -\frac{\mu}{\alpha}\vec{v} \tag{3.15}$$

For the viscous term, the pressure drop is given by

$$\nabla P = -\sum_{j=1}^{3} C_{2_{ij}}\frac{1}{2}\rho|v|v_j \tag{3.16}$$

The inertial term coefficient provides a correction factor for inertial losses in the porous medium. This allows the pressure drop to be specified as a function of dynamic head. To model the flow only transmitted in the axial direction and very negligible in the radial direction, these coefficients are specified much higher in the radial direction than in the axial direction. The resistance direction and hence, the flow direction is specified through direction vectors. The physical properties of the monolith can be specified as anisotropic.

The energy transport equations in this work uses a equilibrium model. This means that the flowing fluid and the porous media are in thermal equilibrium with each other. The properties used are effective properties, that are functions of porosity of the porous media.

To allow for heat transfer between the catalytic converter and the ambient, a shell conduction model is used. The value of thickness of material and the heat transfer coefficient are specified. A tuned value of heat transfer coefficient that is obtained from the measured temperatures from the catalytic converter is used in the simulations, in Paper 1 and Paper 3. Other simulations are adiabatic simulations.

3.3.1 Estimation of porous media resistances

The inertial and viscous resistances can be obtained via experiments. Experimental pressure drop measured at various flowrates is plotted against the flowrate (velocities), as shown in figure 6.2 in the Appendix. An empirical model can be fit to the data with the independent variable as velocity. The coefficients of the linear term and quadratic term give the values of the viscous and inertial resistances respectively.

3.4 Source term for reactions in the monolith

Reactions occur in the catalytic section and porous media approximation is used in all the simulations in this thesis. In an actual monolith, the flow is unidirectional and laminar, with no flow between channels. This is realized in the simulation by specifying large resistances to flow. Viscous and/or and inertial resistances can be inputs to the porous media model for the monolith. In all the simulations, the viscous resistance in the flow direction is specified and a resistance that is larger by three orders magnitude is specified for the non-flow directions. Porosity and material of the catalyst are also specified. Equilibrium is assumed in the porous media representation, which assumes thermal equilibrium in the catalyst.

Both reactive simulations and non-reactive simulations are performed in this work. Kinetic expressions are written using user defined functions (UDF) to represent the species source terms for reactions. The simulations described in Paper 1 and Paper 3 are non reactive, while Papers 2, 4 and 5 involve reactive simulations. The description of the kinetics is described in the next subsections.

3.4.1 First order heterogeneous reaction scheme

In paper 2, to demonstrate the effect of pulsations on the mixed cup species conversions, a first order heterogeneous reaction is specified as source term through an Arrhenius type rate expression as shown below:

$$R = -\bar{Y}\rho SA \exp\left(E_A/R_{gas}T\right), \tag{3.17}$$

where S is the specific area (wall surface available per reactor volume, m^2/m^3), is the Arrhenius frequency factor (1/s), E_A is the activation energy (J/mol), and R_{gas} is the universal gas constant (J/K $\cdot$ mol). The values are $S = 4 \cdot 10^3$ m^2/m^3, $A = 2 \cdot 10^6$ s^{-1} and $E_A = 100$ kJ/mol.

3.4.2 Diesel oxidation catalyst kinetics

Reactions like CO oxidation, C_3H_6 reduction of NO, oxidation of C_3H_6, reversible oxidation of NO and oxidation of H_2 are the common reactions in a catalytic converter, involving species in the exhaust (CO, O_2, C_3H_6, NO, H_2, NO_2, CO_2, H_2O and N_2). Global rate expressions for these reactions are used [75] in reactive simulations in Paper 4 and Paper 5. Reduced order model (ROM) is developed combining CFD solutions and multi variate data analysis (MVDA) procedures such as the principal component analysis (PCA), D-optimal design, multiple linear regression (MLR). To demonstrate the methodology, reactive CFD simulations are performed with oxidation catalyst. The kinetic rate expressions are given in Table 3.1.

Table 3.1: DOC kinetics and global rate expressions by Pandya et al. [75]. X_i represents the mole fraction of species i, k_j are rate coefficients, K_j are adsorption equilibrium constants, and G_j are inhibition terms. R_{gas} is the universal gas constant, T is the temperature (K).

Reaction	Global rate expression (kmol/m_{cat}^2, s)
R1: $CO + \frac{1}{2}\ O_2 \longrightarrow\ CO_2$	$\frac{k_1 X_{CO} X_{O_2}}{G}$
R2: $C_3H_6 + \frac{7}{2}\ O_2 + 2\,NO \longrightarrow 3\,CO_2 + 3\,H_2O + N_2$	$\frac{k_2 X_{C_3H_6} X_{NO} X_{O_2}}{G G_4}$
R3: $C_3H_6 + \frac{9}{2}\ O_2 \longrightarrow 3\,CO_2 + 3\,H_2O$	$\frac{k_2 X_{C_3H_6} X_{O_2}}{G}$
R4: $NO + \frac{1}{2} O_2 \longleftrightarrow NO_2$	$\frac{k_3 \left(X_{NO} X_{O_2}^{0.5} - P^{-0.5} X_{NO_2}/K_{EQ}\right)}{G}$
R5: $H_2\ + \frac{1}{2}\ O_2 \longrightarrow\ H_2O$	$\frac{k_1 X_{H_2} X_{O_2}}{G}$
Adsorption inhibition factors $G = TG_1G_2G_3$ $G_1 = (1 + K_1 X_{CO} + K_2 X_{C_3H_6})^2$ $G_2 = 1 + K_3 (X_{CO} X_{C_3H_6})^2$ $G_3 = 1 + K_4 X_{NO}$ $G_4 = 1 + K_5 X_{O_2}$	
Kinetic Constants $k_1 = 1.93 \times 10^{11} \exp\left(\frac{-51873}{R_{gas}}[\frac{1}{T} - \frac{1}{450}]\right)$; $k_2 = 1 \times 10^{9} \exp\left(\frac{-90000}{R_{gas}}[\frac{1}{T} - \frac{1}{450}]\right)$; $k_3 = 2.83 \times 10^{7} \exp\left(\frac{-21341}{R_{gas}}[\frac{1}{T} - \frac{1}{450}]\right)$; $K_1 = 648.6 \exp\left(\frac{6574}{R_{gas}}[\frac{1}{T} - \frac{1}{450}]\right)$; $K_2 = 2.21 \times 10^{4} \exp\left(\frac{13226}{R_{gas}}[\frac{1}{T} - \frac{1}{450}]\right)$; $K_3 = 5.792 \times 10^{13} \exp\left(\frac{40000}{R_{gas}}[\frac{1}{T} - \frac{1}{450}]\right)$; $K_4 = 3.63 \times 10^{4} \exp\left(\frac{4482}{R_{gas}}[\frac{1}{T} - \frac{1}{450}]\right)$; $K_5 = 3.679 \exp\left(\frac{-67207}{R_{gas}}[\frac{1}{T} - \frac{1}{450}]\right)$; $\ln(K_{EQ}) = 5.0462 + \frac{6343.4}{T} - 2.2973 \ln(T) + 3.0315 \times 10^{-3} T - 8.2812 \times 10^{-7} T^2 + 1.1412 \times 10^{-10} T^3$	

3.5 Description of the geometry

Two specific geometry configurations are used in this thesis. The first geometry, is named as academic muffler, as shown in Figure 3.1. This is used in the simulations reported in Papers 1, 3 and 5. This structure emulates an actual catalytic converter. Vertical section contains the inlet at the top and leads the flow to the horizontal section through a 90° bend. This bend creates a significant flow distribution at the inlet of the monolith. The dimensions of the geometry of the muffler are given in Table 3.2. The horizontal section extends asymmetrically more on the right than the left, The left sections ends as a wall with no outflow. The geometry is partitioned into 700,388 hexahedral cells.

A second structure represented by Figure 3.2 is used in the reactive simulations of Paper 2. Here, a monolith with inlet and outlet cones along with connecting ducts is considered for the reactive simulations. The monolith is 90 cm in diameter and 140 mm long. This central section is connected to 45° cones on either sides. 30 mm pipes transport the reactants and products. The geometry has radial and angular symmetry. A schematic

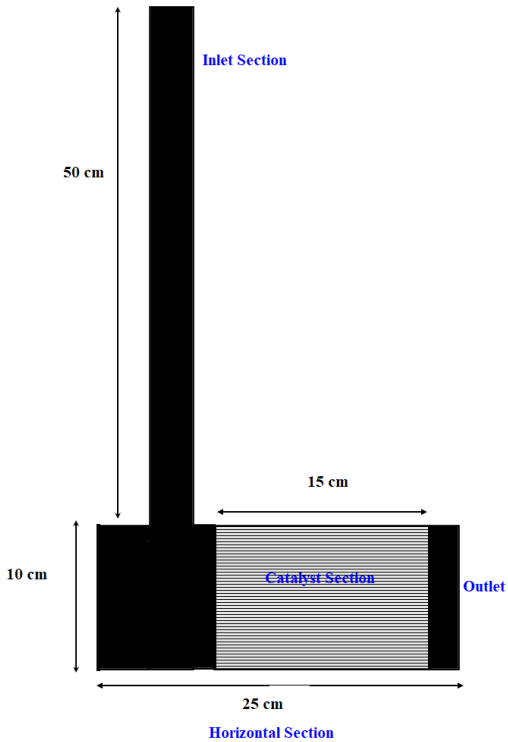

Figure 3.1: *Schematic of the academic muffler for the simulations in Papers 1, 3, and 5. The hatched section represents the catalytic section. The blackened region represents the non-catalytic section. The flow is from top to bottom and from left to right. The domain is half-symmetric (the illustrated cross-section represents a symmetry plane).*

of the geometry is shown in Figure 3.2. The meshed geometry has 11093 cells, with a resolution in the range of $0.06 - 0.6$ mm at mesh-independent conditions.

For the reactive simulations in a DOC, as described in Paper 4, a scaled version of Figure 3.2 is used, preserving the overall structure. The catalyst measures 25.4 mm in diameter and 76.2 mm in length. The length of the converter with cones included is around 220 mm.

Table 3.2: Geometry Details of the Academic Muffler

Parameter	Variable	Value
Diameter of Inlet section	D_{inlet}	3 cm
Length of the inlet section	l_{inlet}	60 cm
Diameter of horizontal section	D_{hor}	10 cm
Length of horizontal section	l_{hor}	25 cm
Diameter of DOC with insulation	D_{cat}	10 cm
Length of DOC (cm)	l_{cat}	15 cm

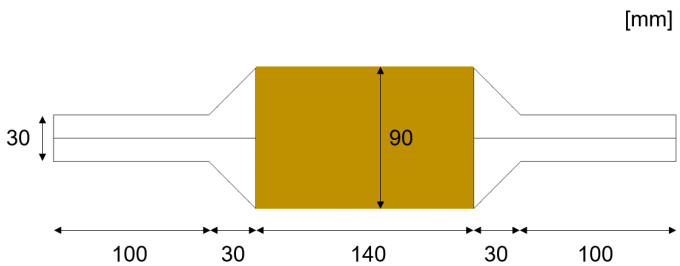

Figure 3.2: *Overview of the computational geometry used for reactive simulations. The flow goes from left to right. The domain is 2D axisymmetric and the horizontal line from the middle of the inlet represents the axis of symmetry. The dark yellow section is the monolith brick.*

3.6 Multivariate Data Analysis

Computational fluid dynamics simulations (CFD) provide velocity, temperature, and species concentrations as functions of time and spatial coordinates. The solution set describing the flow field constitutes a multivariate dataset denoted as (X). Depending on the mesh resolution, total simulation duration, and data logging time steps, the dataset size can become significantly large. Additionally, generating transient CFD solutions is computationally intensive. Therefore, a methodology is necessary to reduce the dimensionality of this CFD dataset (X) while maintaining accuracy. Principal Component Analysis (PCA), a statistical Multivariate Data Analysis (MVDA) technique, serves this purpose [76]. Introduced by Pearson in 1901, PCA has become a standard tool in data analysis [77]. It captures dataset information in terms of covariances through orthogonal linear transformation, expressing them as fewer variables known as "principal components (PCs)" which are orthogonal to each other. For a matrix with K variables and N observations, there will be A PCs, where $A \leq min(K, N)$, which adequately explains the data. The solution set that is termed as data matrix will then be expressed in terms of scores and loadings and a residual matrix.

$$X = TP' + E \approx TP \tag{3.18}$$

Scores help visualize the distribution of data points in the reduced-dimensional space defined by the principal components. Loadings are the coefficients that define the relationship between the original variables and the principal components. They indicate the contribution of each original variable to the creation of the principal components. Loadings help in understanding/identifying the variables that contribute the most to the variation captured by each principal component. The residual matrix represents the part of the original data that is not explained by the retained principal components.It is computed as the difference between the original data matrix and the reconstructed data matrix obtained using the retained principal components.

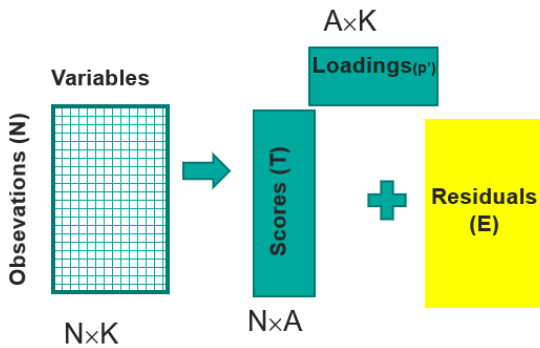

Figure 3.3: *Schematic representation of the PCA. The dataset which is to be dimensionally reduced has a size of $N \times K$. K and N are the number of variables and observations. Scores matrix contains the significant principal components. P and E are the loading and residual matrices.*

Prior to PCA, the solution dataset needs to be scaled. Unit variance (UV) scaling is the scaling method used, where every variable in the matrix is transformed by subtracting column wise mean and normalized by column wise standard deviation [78]. This procedure changes the origin to zero and makes all variables contribute equally to the variance and prevents data points with larger scales from dominating the variance of the model. The scaled solution set, representing the data matrix, is then expressed in terms of a scores matrix and a loading matrix. The resulting matrix will have the same number of rows as the scaled matrix, but reduced to p columns, representing p principal components.

The principal components are arranged such that the first component captures the highest variance within the data, while subsequent components capture diminishing amounts of variance. This arrangement enables a balance between retaining information and reducing dimensionality. The degree of reconstruction depends on the number of principal components retained. Heuristic rules exist to determine which principal components should be retained [79–81]. The identified principal components from the scaled CFD solution data will provide the number of channels that can explain the maximum variance of the dataset. These channels can then be used as representative channels.

3.6.1 D-Optimal Design

D-Optimal design is a concept commonly used in experimental design, and it plays a crucial role in selecting an optimal set of experimental conditions or data points to maximize information about a system [82]. From the scores matrix, a smaller set is chosen, depending on the maximum number of PCs required. This subset is called the candidate set or the information matrix, represented by $\mathbf{X}$. D-optimality criterion states that the determinant $|X^T X|$ should be maximized. With a fixed design size, it can be asserted that an increased determinant of the information matrix implies a dispersion matrix that is more closely aligned with orthogonality. Orthogonality ensures the independence of model coefficients, proving particularly valuable when assessing the significance of these coefficients [83]. D-Optimal design then gives the location of the channels (obtained from PCs).

3.6.2 Weighted Least Squares

Weighted least squares (WLS) regression is the final step in model reduction and MCM. A common assumption in both linear and non-linear regression is that each data point contributes equally precise information to the model. This implies that the dataset has a constant standard variation. However, this assumption may not be valid in many applications. For example, in the CFD solution dataset, the center regions of the monolith might have a different temperature and flowrate than the walls. This variation will be pronounced in cases of flow maldistribution. In these situations, where treating every observation equally may not be reasonable, weighted least squares often proves beneficial for enhancing the efficiency of parameter estimation [84]. This involves assigning each data point an appropriate level of influence over parameter estimates, recognizing that a uniform treatment of all data points could disproportionately impact less precisely measured points and inadequately influence highly precise points. Regression is applied on the specific channels picked up by the D-optimal design, on a weighted basis.

An objective function y represents the response variable, that we aim to predict for the multichannel model. This response variable y is typically a function of several variables that are a part of the CFD solution set. For example, consider the response variable y representing the heat content of the fluid on any plane. The heat content Q can be expressed as product of mass flowrate, specific heat capacity and the temperature difference of the fluid over the reference temperature. The mass flowrate is the product of area, velocity and density. All these are obtained from the solution set.
The predicted variable $\hat{Y}$, for a multichannel model, is the weighted average of the objective function at the channels given by the D-optimal design. The response variable $(\hat{Y})$ is expressed as the product of weights and function of the solution variables (X), and differs from the exact solution by the error (ε), as given by

$$\hat{Y} = X\hat{\omega} + \varepsilon$$

The goal is to find the weights $(\hat{\omega})$ that minimizes the sum of squared residuals

$$\min_{\omega} ||\hat{Y} - X\omega||_2^2$$

The estimates of $\hat{\omega}$ are obtained by least squares regression and are given by:

$$\omega = (X^T X)^{-1} X^T Y$$

Thus, the combination of scaling, PCA, D-optimal design and weighted least squares on the full CFD solution forms the basis of the MCM.

3.6.3 Working Procedure

An in-house code is written in MATLAB for PCA. First, CFD solution is collected and arranged in the required form of observations and variables at the catalyst outlet, as this plane of the catalyst is of interest. From the set of nodes (cell centers) at which the data are collected, a subset of the nodes become the principal components, this is the output from PCA. NIPAL's algorithm is the method used in getting the principal components [85]. Scaling, checking for columns that have zero variance and iterative method of getting scores and loading values are coded and the output of the PCA code is the number of principal components.

The scores matrix is the input (candidate set) for the D-optimal design procedure. Here, `candexch` function of MATLAB is used to identify the exact nodes (channels), with the maximum number of iterations specified [86]. The size of the scores matrix on which D-optimal design procedure is applied depends on the principal components. Least squares regression is performed on the objective function and weights are the output from the regression. Heat content of the fluid and species conversion can be used as objective function. Metrics like residuals and root mean square of the error are used to quantify the efficiency of the model.

3.7 Single Channel Model

A catalytic converter, also known as honeycomb monolith, consists of hundreds of parallel channels, with walls coated with active catalytic material. The fundamental assumption of the single channel model is that all these channels are identical and the flow through each of the channels is equal. Further, the inlet conditions at each of these channels is identical. The walls are impervious to flow, but can conduct heat by conduction. Therefore, only energy is transferred between channels, but not mass. Heat transfer is possible by convection (inside the channels) and by conduction (through the walls) and by radiation. In SCM, the radial heat transfer in the channel and thermal interaction between channels are neglected. The flow within the monolith is primarily laminar. The monolith's behavior is depicted using a pseudohomogeneous model for reactions, wherein the bulk species concentration is assumed to be equal to concentration of the species on the (catalytic) wall. This approach aligns with the porous media assumption adopted in the Computational fluid dynamics (CFD) model. Additionally, the solid temperature is assumed to be same as the gas phase temperature, and is similar to the thermal equilibrium assumption in the CFD model.

The species and energy balance equations for a single channel under transient conditions are given by [87]:

$$\frac{\partial C_i}{\partial t} + \frac{\partial \left(uC_i\right)}{\partial z} = \nu_{ij} R_j \tag{3.19}$$

and

$$\frac{\partial \left[\varepsilon\rho_g + C_{p,g} + (1-\varepsilon)\rho_s C_{p,s}\right] T}{\partial t} + \frac{\partial \left(u\rho_g C_{p,g} T\right)}{\partial z} = \nu_{ij} R_j \Delta H_{r,j} \tag{3.20}$$

where, C_i is the concentration of species i (mol/m^3), u is the axial velocity of the fluid through the catalyst channel (m/s), z is the axial coordinate direction, ε is the volume fraction of gas (-), T is temperature (K), and subscripts g and s refer to *gas* and *solid*, respectively.

3.7.1 Tanks-in-series model

A tubular reactor like the single channel of the monolith can be solved using tanks-in-series model [88] as shown in Figure 3.4. The partial differential equations as in 3.19 and 3.20 will be converted to ordinary differential equations (ODE), as the model is a 0D-model, where the concentrations and temperature in any tank is a function of time alone. The size of the tank is identical to the number of cells in the catalyst in the CFD mesh, this ensures identical numerical dispersion in both 1D-SCM and 3D-CFD models.

The initial and boundary conditions applied here as same as in the CFD models.

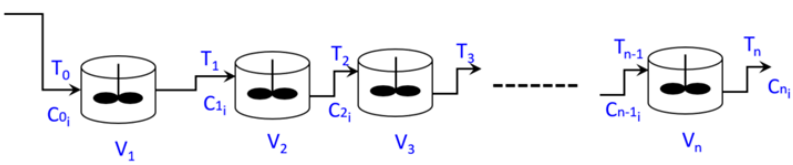

Figure 3.4: *Reactor Volume V is assumed to be composed to n tanks having equal volume. Tanks are completely mixed, the concentration of species and the temperature of the gas phase is a function of time alone.*

The species and energy balance equations in the tanks-in-series representation are:

$$\frac{dC_{i,n}}{dt} = \frac{q}{V_t}(C_{i,n-1} - C_{i,n}) + \Sigma_{j=1}^{nrxn} \nu_{ij} R_{j,n} \tag{3.21}$$

and:

$$\frac{d}{dt}\left[\varepsilon\rho_g C_{p,g} + (1-\varepsilon)\rho_s C_{p,s}\right] T = \frac{q}{V_t}\rho_g C_{p,g} T_{n-1} - \frac{q}{V_t}\rho_g C_{p,g} T_n + \Sigma_{j=1}^{nrxn} \nu_{ij} R_{j,n} \Delta H_{r,j} \tag{3.22}$$

Here, q is the volumetric flow rate (m^3/s) corresponding to u in the governing PDEs, V_t is the volume of a tank (obtained by dividing the total catalyst volume by the total number of tanks in series), and subscripts n and $n-1$ refer to the current and upstream tank, respectively. For the first tank, $C_{i,n-1}$ and T_{n-1} are given by the inlet boundary conditions. The rate expressions used in this work for 1D-SCM are given in Table 3.1.

3.8 Nonlinear least squares regression

In a chemical reactor, the species conversion is a nonlinear function of the reaction rate and the residence time. Reaction rate is generally expressed in terms of Arrhenius form, as a function of temperature and concentration of the reactant. This is given by

$$\chi_i = f(v, e^{\frac{-E_a}{RT}}, [C_A]^a) \tag{3.23}$$

where χ_i is the conversion of species and is defined as $\frac{(C_{A_0} - C_{A_i})}{C_{A_0}}$, which is the ratio of moles of reactant A reacted to that of moles of A fed initially. v is the residence time, E_a is the activation energy, R_{gas} is the universal gas constant and T is temperature. $[C_A]^a$ is functional form of species concentration.

SCM assumes flow to all channels is uniform and every channel experiences uniform inlet conditions. Under adiabatic conditions, the heat of reaction, if exothermic, heats up the gases to increase the temperature. When there is flow maldistribution, some of the channels experience a larger flow, and some channels experience a smaller flow. This causes differences in inlet temperatures and residence times. Hence, the conversion is a function of the flow maldistribution in addition to residence time and temperature as given in Eq. 3.23.

The conversion in more realistic systems is a mass weighted average of spatially distributed concentration at the outlet. Applying SCM to realistic system will have different outlet predictions as radial heat transfer is not accounted for in the SCM and the assumption of uniform inlet conditions. This will then predict conversions different from the 3D models. At constant temperature, a pseudo-channel model can be envisaged as a SCM that will give same conversion as the system with flow maldistribution, at a different residence time.

Thus, for realistic systems with flow maldistribution,

$$\chi_i = f(v, e^{\frac{-E_a}{R_{gas}T}}[C_A]^a, geometry) \tag{3.24}$$

The objective function can then be formulated as follows: find the residence time of a SCM that will provide the same conversion of chosen species at steady state reactive conditions at constant temperature.

$$v_{\mathrm{SCM}} = \min \sum_{i=1}^{n_{\mathrm{sp}}} f(\chi_{i\mathrm{CFD}} - \chi_{i\mathrm{SCM}})^2 \tag{3.25}$$

As the conversion is a non-linear function of residence time and temperatures, Levenberg-Marquardt algorithm can be employed to obtain the solution of Eq. 3.25. This algorithm is widely employed in nonlinear least squares optimization [89, 90]. It combines the advantages of Gauss-Newton Algorithm and gradient descent algorithm, by interpolating between these two approaches, making it particularly effective for minimizing the sum of squared differences between observed and predicted values. At each iteration, the algorithm calculates a step direction by combining the Gauss-Newton step (which is efficient but can be unstable) and the gradient descent step (which is stable but slow). The Levenberg-Marquardt method introduces a damping parameter that controls the trade-off between these two steps, allowing for adaptive adjustments based on the local curvature of the objective function. The algorithm iteratively updates the parameters of the model until convergence criteria are met, typically by minimizing a merit function that quantifies the discrepancy between observed and predicted values.

In the formulation of pseudo-channel model, the objective function is given by Eq. 3.25 and is solved using `lsqnonlin` function in MATLAB [91]. This method needs an appropriate initial guess and bounds are not needed to be specified. The initial guess for the Levenberg algorithm can be the mixed cup values at the inlet of the catalyst from the CFD results.

3.9 Detached eddy simulations

The RANS equations are presented in Section 3.2. The RANS equations operate under the assumption that all variables can be decomposed into mean (time-averaged) and fluctuating components. RANS models require the specification of turbulence closure models, which introduce additional uncertainties and assumptions into the simulations. Large Eddy Simulations (LES) use volume averaging, unlike RANS. LES directly simulate or resolve the larger turbulent structures while modeling the smaller scales. This allows for a more accurate representation of turbulent flows, particularly in regions where large-scale, unsteady phenomena play a significant role. Detached eddy simulations (DES) is a blend of both LES and RANS models, where RANS is applied near the boundary layers (walls) and LES to resolve large eddies.

The SST $\kappa - \omega$ model of turbulence is used in DES too. For RANS, the length scale is proportional to $\frac{\sqrt{\kappa}}{\omega}$ and that in LES is the mesh resolution Δ. When the mesh is sufficiently fine, enabling the DES switching from RANS length scale at the walls to a

LES length scale at the bulk is done by a new blending function F_{DES} by changing of the term $\beta^*\kappa\omega$ in the κ equation of SST - $\kappa - \omega$ model, to $\beta^*\kappa\omega F_{DES}$, where F_{DES} is given by:

$$F_{DES} = \max\left\{\frac{L_t}{C_{DES}\Delta}, 1\right\} \tag{3.26}$$

where $L_t = \dfrac{\sqrt{\kappa}}{\beta^*\omega}$ and $\Delta = \max\{\Delta x_1, \Delta x_2, \Delta x_3\}$. The value of β^* and C_{DES} are 0.09 and 0.61 respectively.
By implementing this modification, one can ensure that the appropriate turbulence scales are being modeled rather than resolved. As illustrated in Equation 3.26, the parameter Δ defines the grid location where the transition between RANS and LES takes place, emphasizing the importance of selecting a suitable grid.

4 Results and Discussion

This chapter provides a summary of the key findings presented in the included papers as a short summary of every paper. A table summarizing the simulations is presented in Table 4.1. An overview of the operating conditions (inlet profiles, boundary conditions and initial conditions) are presented first, the discussions and results follow later.

Table 4.1: Summary of inferences in the included papers

Paper #	Simulations	Geometry	Inference
I	Non Reactive	Geometry 1	Histogram of Temperature and Velocity, Limitation of SCM under Flowmaldistribution
II	Reactive	Geometry 2	Effects of inlet pulsations on mixed cup conversions at catalyst outlet
III	Non Reactive and DES, Steady State	Geometry 1	Applicability of RANS
IV	Reactive and MVDA	Geometry 2	Methodology of reduced order model development using DOC kinetics
V	Reactive, Steady state and Transient	Geometry 1	Methodology for pseudo-channel model using steady state reactive simulation and using nonlinear least squares optimization for EATS with flow maldistribution

4.1 Summary of Paper I - Transient flow uniformity evolution in realistic exhaust gas aftertreatment systems using 3D-CFD

Paper I is focused on demonstrating the limitations of the Single Channel Model. It also explains the analysis of flow non-uniformity as histograms and contours. A complex geometry with a 90° bend and a partial dead volume is the chosen geometry. Transient step input is applied to the inlet of the geometry. The evolution of the flow field and temperature field is obtained through the solutions of Unsteady Reynolds-Averaged Navier Stokes Equations for continuity, velocity and temperature. The catalyst section is modeled using porous media model. The resistances that are used in the porous model are obtained through the flow - pressure drop measurements done on the experimental rig, with hot air at various flowrates. The heat loss magnitude is also obtained by logging temperatures at several locations at the inlet and outlet of the monolith using thermocouples. These measurements gave an estimate of the heat transfer coefficient value for describing heat loss.

4.1.1 Operating conditions and simulation cases

Two sets of transient simulations are designed to study the evolution of uniformity the development of flow field. The operating conditions are shown in Table 4.2.

Table 4.2: Operating Conditions

Flow parameter	Steady state 1	Steady state 2
Volumetric Flowrate at STP (lpm)	500	948
Operating Temperature (°C)	100	93
Velocity at Operating conditions (m/s)	11.8325	22.0135
GHSV of the catalyst (h^{-1})	39189	74302
Residence time (s)	0.181	0.097

4.1.2 Boundary conditions

The inlet boundary conditions are listed in Table 4.3. A step change is introduced at $t = 0s$ and $t = 20s$ in the two cases to a velocity of 22.0135 m/s from 0 s and 11.8325 s respectively for the first and second simulation. The changes are also effected in the inlet temperature. The simulation is performed until steady state is attained in both cases. Turbulent intensity of the order of $I_{turb} = 0.16Re^{\frac{1}{8}}$ and length scale at 7 % of the hydraulic diameter are specified as inlet turbulent conditions. Temperature and velocity are passed through time dependent user defined function (UDF) to the simulation.

Pressure outflow is specified at the outlet boundary condition, with zero gauge pressure. The backflow turbulent intensity and viscosity ratio are set at 5 and 10 % respectively. Walls are specified with no-slip boundary condition. Symmetry plane reduces the computational load.

Table 4.3: Simulation cases

Case name	0 to SS1	SS2 to SS1
Starting time (s)	0	0
Initial velocity (m/s)	0	11.8325
Initial Temperature (°C)	20	100
Step Change Time (s)	0	20
Velocity at Step Change (m/s)	22.0135	22.0135
Temperature at Step Change (°C)	93	93
Simulation Stop time (s)	35	35

4.1.3 Solution methodology

The symmetry plane is located in the middle plane of the muffler. Iterative solution strategy for handling the pressure velocity coupling by the semi-implicit pressure linked equation (SIMPLE) method. First order upwind scheme is used for discretising the convective terms. Second order accurate central differencing scheme is used for diffusional

terms. Under relaxation factors were used for pressure, momentum, specific dissipation rate and turbulent kinetic energy. Default values were retained for the turbulent model constants and the damping functions. Convergence was ensured when the residuals dropped to atleast three orders of magnitude from the starting values. Refinement of the grid was done in the regions that showed substantial gradients. A timestep of 0.005s is chosen for the solution scheme.

4.1.4 Temperature and velocity histograms

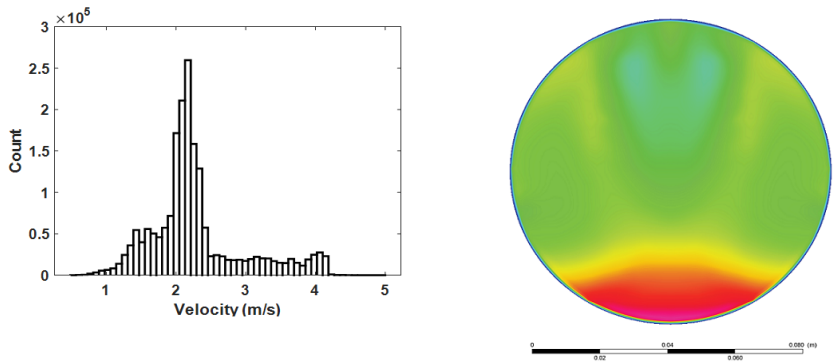

Figure 4.1: *Histogram of velocity over the monolith (left) and contour of velocity in the center plane of the monolith at the end of 35s.*

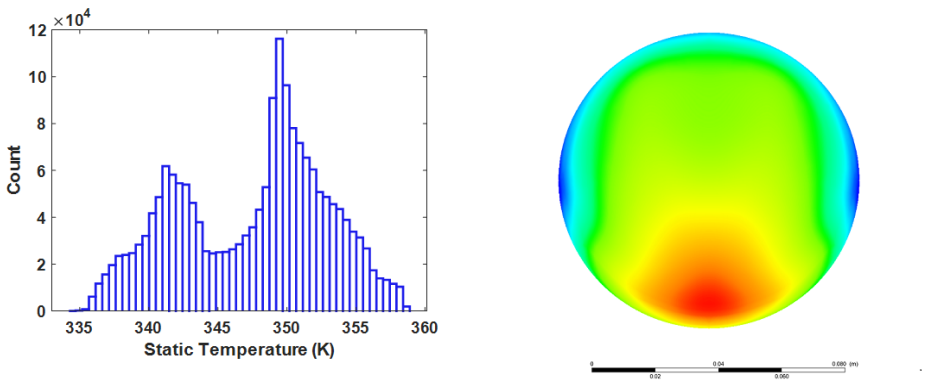

Figure 4.2: *Histogram of temperature over the monolith (left) and contour of temperature in the center plane of the monolith at the end of 35s.*

In the simulations, hot air at a certain velocity and temperature is passed over a cold catalyst. Heat loss from the muffler to the ambient is specified using a heat transfer

coefficient. One important aim of this work is to understand the interaction of the flow field with the temperature field. The fluid in the flow straightener emerges as a jet and the lower section experiences a larger flow than the upper section in the horizontal section of the muffler. The flow then squeezes into the monolith and emerges out. The heating of the muffler along with monolith competes with the heat loss from the muffler. The pressure drop experienced by the flow and the heat loss aid the evolution of uniformity. This process is captured by the contours at three locations inside the monolith and at the exit. Velocity and temperature contours show the circulation of heat inside the monolith in Figures 4.1 and 4.2. This variation is captured spatially and temporally.

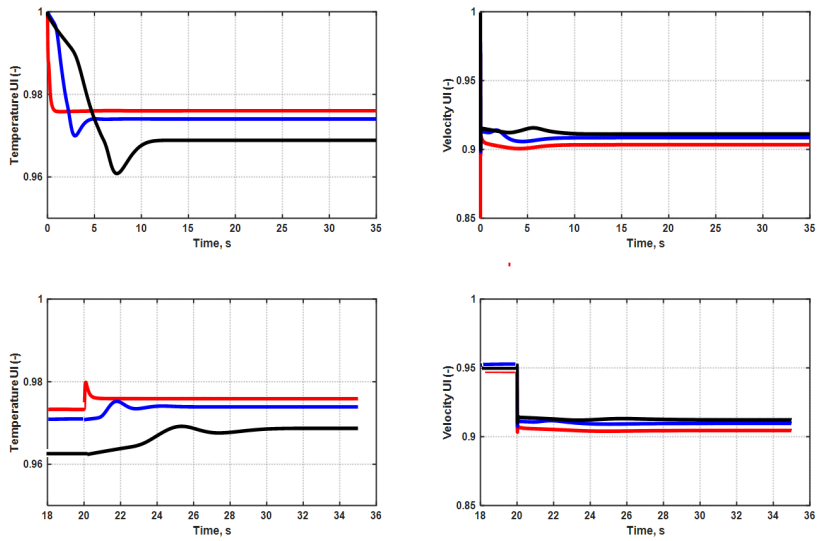

Figure 4.3: *Transient variation of uniformity indices. The top panels (a) and (b) represent the temperature and velocity UI plots for the simulation* `0 to SS1` *case and the lower panels (c) and (d) represent the same for the simulation* `SS2 to SS1`*. The location of the red line is at the entry of the catalyst, blue and black are the planes in the middle and outlet of the catalyst respectively.*

The histograms and contour plots of velocity and temperature illustrate a lack of uniformity in both the velocity field and temperature distribution. Moreover, the distribution displayed in the histograms is influenced by the inlet temperature and velocity. Due to this wide-ranging distribution, relying on a single representative channel within the SCM to explain the behavior of all channels, especially under transient conditions, will be limited in accuracy.

Another important outcome of this study is the implication of the value of uniformity index. In the study, a value of uniformity index was obtained for velocity and temperature. Identical values of UI does not mean identical levels of uniformity of flow field and

temperature fields. A plot of UI for velocity and temperature for the two simulations cases is shown in Figure 4.3. The value of UI is decreases with increase in velocity. Lower temperature values improve uniformity. The flow parameters at the inlet increase in velocity, but decrease in temperature at t = 0. The UI value for temperature improves to a higher value whereas there is a dip in velocity UI.

4.2 Summary of Paper II - Numerical assessment of flow pulsation effects on reactant conversion in automotive monolithic reactors

Transient reactive simulations were carried out with the inlet velocity varying with time as specified graphically in Figure 4.4. The effect of the inlet pulsations on the mixed cup species conversion is studied.

4.2.1 Boundary conditions

The inlet pulsations are specified as a constant inlet velocity, a square inlet velocity, a sinusoidal inlet velocity and a triangular inlet velocity. The variations are specified either as a velocity inlet or as a pressure inlet. Inlet reactant concentration is also specified as mass fraction. The outlet conversion is calculated using $X = 1 - \bar{Y}_{out}/\bar{Y}_0$, where $\bar{Y}_{out}$ is the mass-weighted average of the reactant mass fraction on the system outlet.

4.2.2 Solution Methodology

The simulations are solved using a double precision based solver, on a colocated grid. The temporal derivatives are discretised by a implicit discretisation. A coupled scheme is used to handle pressure-velocity coupling . Convective terms are discretised using a third order Monotonic Upstream-centered Scheme for Conservation Laws (MUSCL) scheme. The diffusion terms are discretised using a second order central differencing scheme. Reaction source terms are handled explicitly. Time step is chosen as 0.001s, to ensure that it is significantly smaller than pulsating frequencies.

Figure 4.5 shows the variation of reactant conversion as a function of time for the cases 1, 2, 3 and 4. Table 4.4 shows the time-averaged conversion, UI for all the eight cases. From the Figure 4.5 and the Table 4.4, the time-averaged conversion and UI are different for the various inlet velocities. There are subtle variations within a case, when the inlet flow is specified as velocity inlet or a pressure inlet. The retention time and specification method affects the conversion at the outlet. In these cases, the extremum points in velocities do not coincide with the extrema in the conversion. The dispersion mechanisms, the movement of plug within the monolith and the eventual mixing in the end cones strongly affect the outlet conversion.

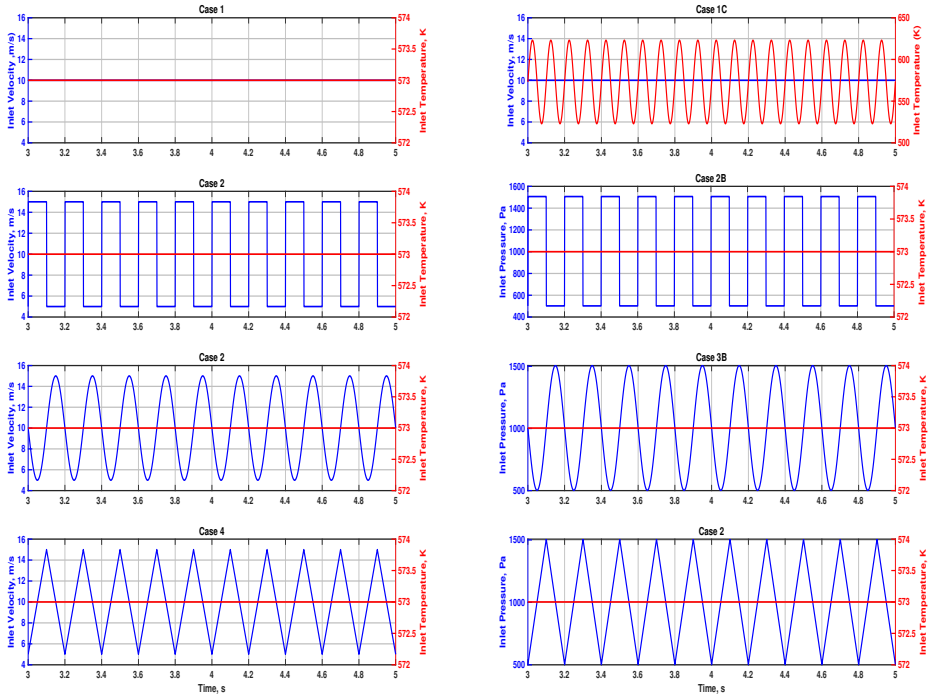

Figure 4.4: *Inlet velocities and temperatures over time as obtained in cases 1, 2, 3 and 4. The blue lines and the red lines represent velocity and temperature respectively.*

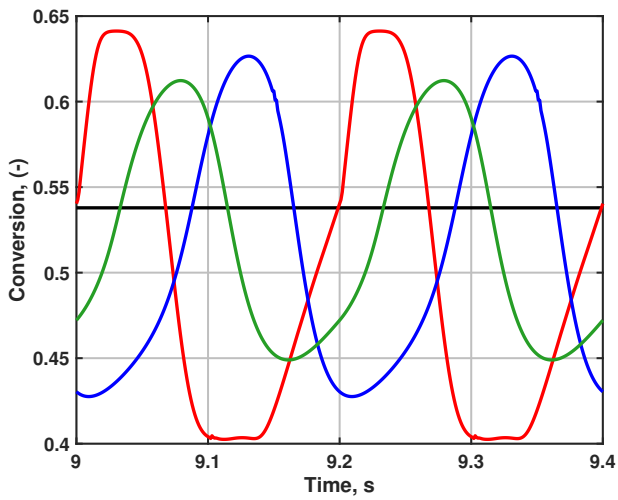

Figure 4.5: *Conversion of Reactant at the system outlet over time as obtained in cases 1 (black), 2 (red), 3 (blue) and 4 (green).*

Table 4.4: Time-averaged results for inlet velocity, conversion at system outlet and uniformity index inside the monolith brick. The variation intervals reported are the standard deviations. Averages and standard deviations are recorded for the last second of a 10-second run.

Case	**Velocity** [m/s]	**Conversion**	**Uniformity index**	**Temperature** [K]
Case 1	10.0	0.538	0.9967	573.0
Case 1C	10.0 ± 0.00	0.498 ± 0.001	$0.9971 \pm 1.64 \cdot 10^{-4}$	573.0 ± 35.36
Case 2	10.0 ± 5.00	0.503 ± 0.090	$0.9966 \pm 2.79 \cdot 10^{-4}$	573.0
Case 2B	9.60 ± 4.52	0.519 ± 0.085	$0.9966 \pm 2.45 \cdot 10^{-4}$	573.0
Case 3	10.0 ± 3.54	0.514 ± 0.073	$0.9967 \pm 8.71 \cdot 10^{-5}$	573.0
Case 3B	9.66 ± 3.25	0.528 ± 0.069	$0.9967 \pm 8.83 \cdot 10^{-5}$	573.0
Case 4	10.0 ± 2.89	0.522 ± 0.060	$0.9967 \pm 6.19 \cdot 10^{-5}$	573.0
Case 4B	9.68 ± 2.66	0.535 ± 0.056	$0.9967 \pm 6.41 \cdot 10^{-5}$	573.0

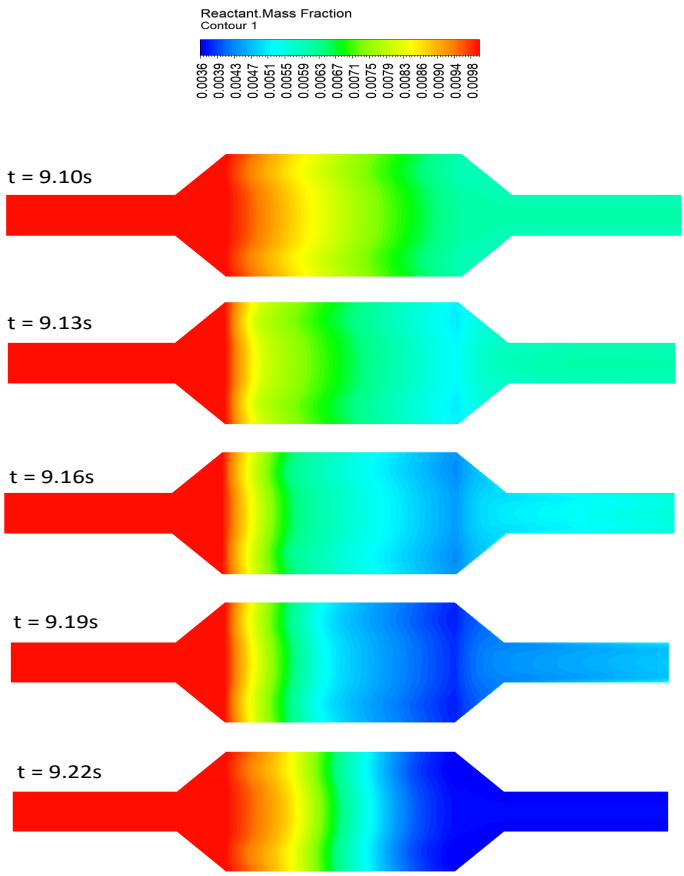

Figure 4.6: *Five snapshots of the reactant mass fraction fields for case 2 (at $t = 9.10$ s, $t = 9.13$ s, $t = 9.16$ s, $t = 9.19$ s, and $t = 9.22$ s).*

Figure 4.6 shows the movement of the reactant plug in the axial flow direction at various times as contours for the case where the inlet velocity is varying sinusoidally (Case 2).The inlet velocity decreases from 10 m/s to 5 m/s at $t = 9.10$ s and increases to 10 m/s again at $t = 9.20$ s. The existence of a low-mass-fraction region emerging from the end of the monolithic reactor is clearly visible at times $t = 9.13$ to 9.19 s, indicating that the reactant mass fraction is not monotonically decreasing along the streamwise direction when the inlet velocity is fluctuating. The times at which low reactant concentration stream emerges is between the times 9.13 to 9.19s. The other times show somewhat higher reactant concentrations. The flushing rate of the reactants is influenced by the inlet velocity.

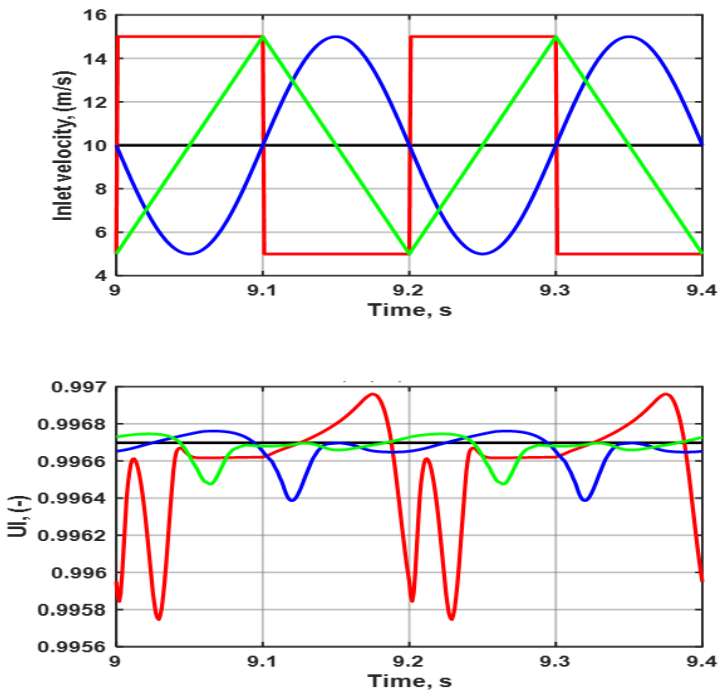

Figure 4.7: *Inlet velocity (upper panel) and Uniformity index of reactant field half-way through the monolith brick (lower panel) over time as obtained in cases 1 (black), 2 (red), 3 (blue) and 4 (green).*

Figure 4.7 shows the temporal variation of uniformity index based on reactant concentration for the simulation cases 1, 2, 3 and 4, along with the inlet velocity variation over time from 9 to 9.4s. The local variation of uniformity indices strong variation depending on the specification of inlet velocity. The UI remains constant with time, only in the case of a constant inlet velocity. All other time dependent inlet velocities show

strong variation of UI. Lower velocities yield high UI and better uniformity in reactant concentration. It is also interesting to note that the peaks and valleys in the UI are out of phase with the inlet velocity. The variation in UI is strongest for pulse inlet velocity specification than the other time varying velocities. The dispersion mechanisms influence the UI and conversion in a non-trivial way, that are very distinct functions of the time dependent inlet velocities.

4.3 Summary of Paper III - Turbulent uniformity fluctuations in automotive catalysts – A RANS vs DES assessment

The primary aim of Paper III was to evaluate the applicability of RANS simulations in comparison to DES. This evaluation focused on assessing the differences in uniformity indices of mean flow between DES and RANS simulations. Additionally, the study aimed to investigate the magnitudes of fluctuations in uniformity index induced by turbulence under specified steady state conditions. Furthermore, the research aimed to assess the cost and utility associated with using DES instead of RANS. The parameters set in the RANS and DES simulations are shown in Table 4.5.

Table 4.5: Summary of initial and boundary conditions and solver settings in the RANS and DES simulations.

Setting	RANS	DES
Turbulence model	SST k-ω	SST k-ω based
Inlet Velocity (m/s)	25	25
Inlet Temperature (K)	423	423
Wall Flow Modeling	Standard Wall Treatment [24]	Standard Wall Treatment [24]
Wall energy boundary condition	Heat losses through shell conduction and an external heat transfer coefficient matched to experiments	Heat losses through shell conduction and an external heat transfer coefficient matched to experiments
Outlet gauge pressure	0 Pa	0 pa
Outlet boundary condition for other quantities	Zero gradient	Zero gradient
Time stepping	None (steady state)	$\Delta t = 0.0001s$
Solver	Coupled	Coupled
Temporal discretization scheme	None (steady state)	Bounded Second Order Implicit
Discretization scheme for convective terms	First Order Upwind	Bounded Central Differencing
Discretization scheme for diffusive terms	Central Differencing	Central Differencing
Fluid	Air	Air

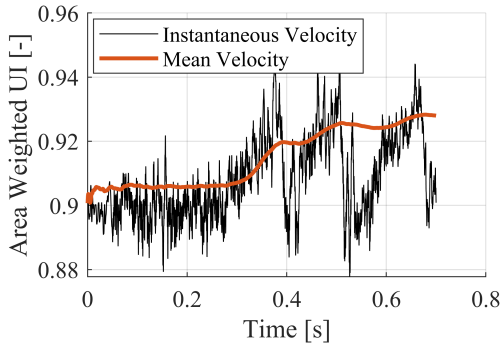

Figure 4.8: *Area-Wighted uniformity index of mean and instantaneous velocity in the middle of the catalyst ($z = 0.1$). $t = 0$ is the time at which statistical sampling was initialized.*

The DES solution exhibits fluctuations of varying amplitudes and frequencies. Figure 4.8 illustrates high-frequency fluctuations with an amplitude of approximately 0.03 in the UI. Additionally, lower frequency fluctuations with an amplitude of around 0.06 are also observed in the figure.

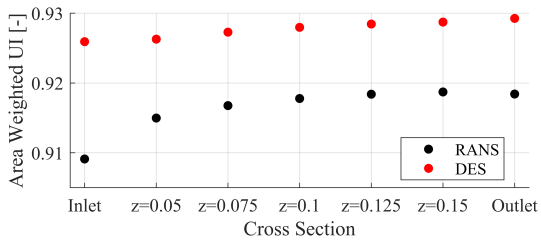

Figure 4.9: *Comparison between RANS and DES results - Area-Weighted uniformity index of mean velocity across the seven cross-sections within the monolith.*

The findings indicate that across all monolith cross-sections, DES simulations yield a more uniform flow compared to RANS simulations as in Figure 4.9. The difference in uniformity index (UI) ranges between approximately 0.010 and 0.015 across all cross-sections. However, as depicted in Figure 4.8, there may be occasional oscillations present at timescales exceeding the temporal scope of the conducted simulation. Moreover, the same figure illustrates that the regular oscillations (approximately 0.03) are at least twice the magnitude of the difference between the averaged DES and RANS results (approximately 0.015) for the uniformity index. Following Equation 2.1, the the deviation in the flow from the mean is 15 % and 17% for RANS simulations and DES respectively and the difference is 2%.

4.4 Summary of Paper IV - Methodology for reduced-order multi-channel modeling of a catalytic converter

The aim of the Paper IV was to develop reduced order models combining solutions from transient reactive CFD simulations and multivariate data analysis techniques. Transient reactive CFD simulations are carried out on a catalytic converter with the geometry shown in Figure 3.2. The catalytic converter is fitted with 45° cones at the inlet and outlet. Global kinetics accounting for the oxidation of carbon monoxide, hydrogen, hydrocarbon (propylene), nitric oxide are adapted from the work of Pandya et al. [75] for a Diesel Oxidation Catalyst (DOC). The space- and time-resolved state variables at the catalyst outlet are then approximated using Principal Component Analysis (PCA) [76]. By applying a D-optimal design criterion on the resulting score matrix, a few representative channels are selected to be combined to predict the mixed-cup average values from CFD. Thus, this combination of CFD, PCA and D-optimal design offers dimensional reduction, yet has the potential to preserve the core features from a full CFD prediction, as shown in Figure 4.10.

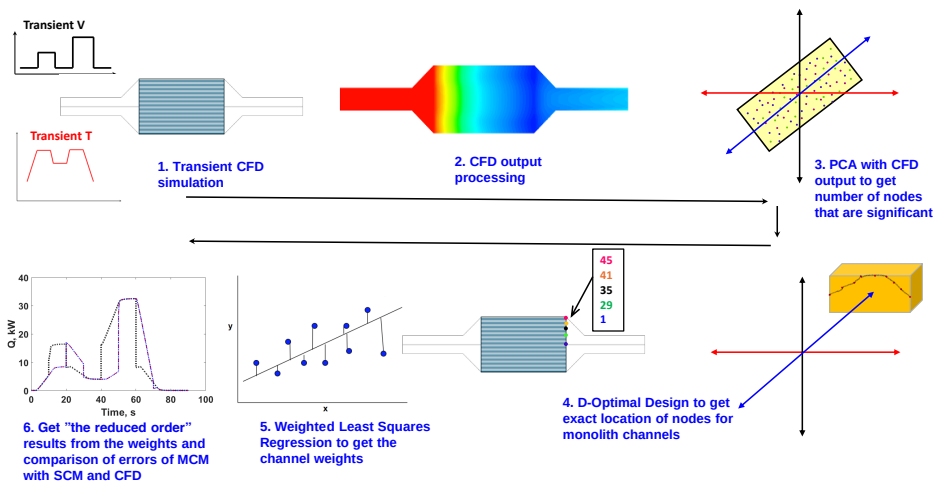

Figure 4.10: *Schematic representation of the reduced order model development process.*

The calibration case includes temperature and velocity transients. A time-shifted transient of the calibration case serves as the test case. Figure 4.11 shows the results of multi-channel model with five retained principal components. Here, conversions of the three species, namely, CO, C_3H_6 and NO are plotted against time for CFD, MCM and SCM. The predictions of MCM match very closely with that of CFD and better than the SCM predictions. Additional test cases with variable species concentration profiles were

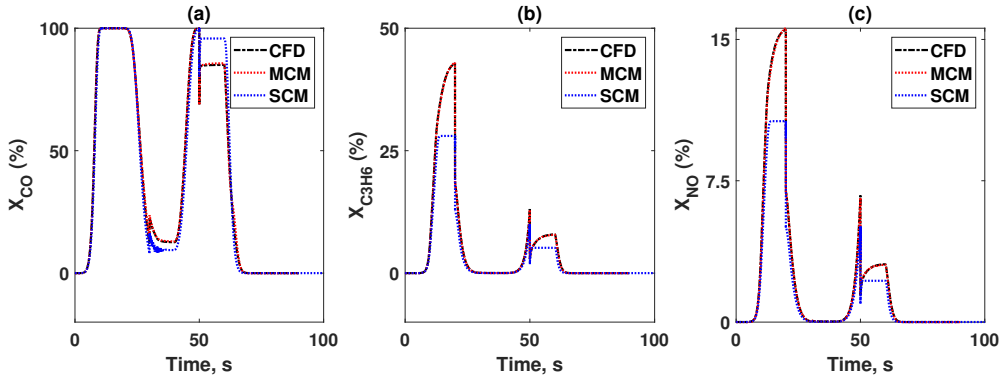

Figure 4.11: *Species conversion prediction using PCA, D-optimal design and weighted least squares - Comparison of CFD, MCM and SCM for the time shifted case and constant species concentration at the inlet, predicted values of species conversion plotted against time. Five principal components were retained. Panels (a), (b), and (c) show the percentage conversions for CO, C_3H_6, and NO, respectively. MCM predictions match accurately with that of CFD predictions and better than the SCM predictions.*

also predicted from the calibration set. The heat content and species (CO, C_3H_6, NO, and H_2) conversion are used as predictor variables. The results of the full CFD simulation are compared with the results predicted of reduced model, in terms of the root mean square error (RMSE) as in Figure 4.12.

4.4.1 Computational efficacy of MCM

The simulations for Paper 4 were carried out on a desktop computer installed with an i7 processor and RAM capacity of 64 GB. Fixed time-stepping was used for all the transient simulations. Depending on the transient inlet conditions (constant vs variable inlet concentration), the completion time for CFD simulations were about 17-27 hours per case. 1D-SCM simulations were solved using MATLAB ode15s solver and required 2.5 - 19.2 minutes for completion per case. With the available CFD output data, the processes of data preparation for MVDA, PCA, D-optimal design and least squares regression required 2 minutes for the combined steps. Thus, MCM is feasible with available data, which can be obtained from CFD or from measurements. MCM has clear advantages in terms of computational efficiency and accuracy.

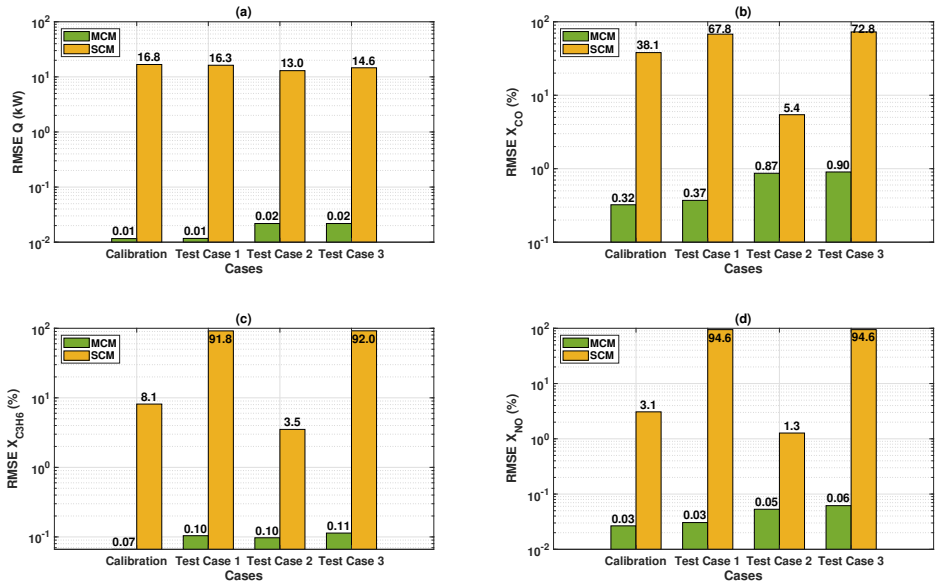

Figure 4.12: *Performance comparison of the developed MCM and the 1D-SCM against the 3D-CFD for heat content and species conversion. Panels (a), (b), (c), (d) are the RMSE comparisons for the heat content, conversions of the species CO, C_3H_6 and NO respectively. Logarithmic axis is used as the SCM RMSE is much larger in magnitude than the RMSE of the MCM.*

4.5 Summary of Paper V - A reduced-order pseudo-channel model accounting for flow maldistribution in automotive catalysis

In realistic systems, the inlet and outlet planes of the catalyst have a distribution of flowfield, unlike uniform distribution assumed by 1D-SCM. A probability density function plotted against the velocity at the inlet and outlet is shown in Figure 4.13. The distribution has variation depending on GHSV and temperature values. This distribution translates as distribution of species conversions at the catalyst outlet.

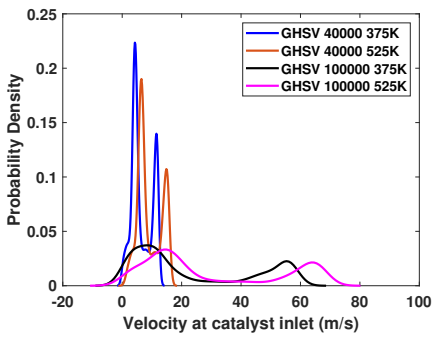

(a) *Distribution of velocity at the inlet plane of the catalyst.*

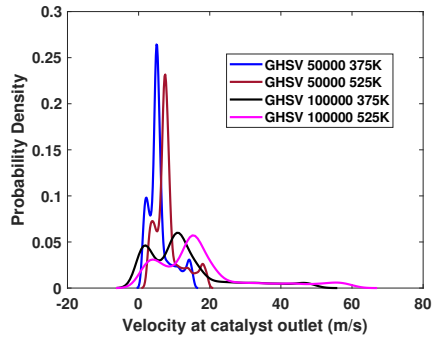

(b) *Distribution of velocity at the inlet plane of the catalyst.*

Figure 4.13: *Distribution of the velocity at the inlet and outlet planes at low and high values of GHSV and temperature.*

4.5.1 Mapping of 3D-CFD with 1D-SCM to obtain pseudo-channel model

A pseudo-channel is envisaged that provides the same species conversion as the 3D-CFD, by formulating an objective function which is the difference of species conversions of

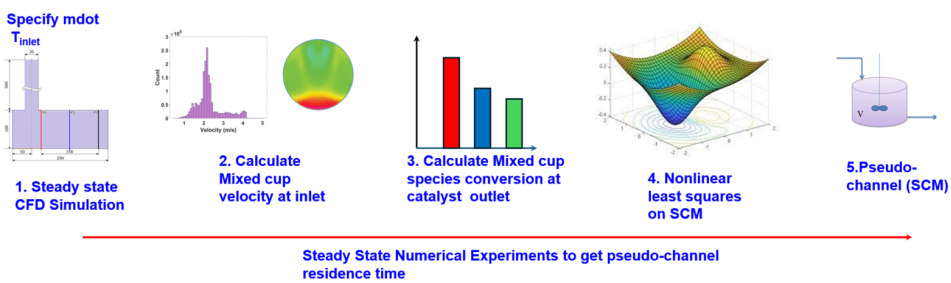

Figure 4.14: *Schematic of steps in the steady state reactive simulation sequence.*

3D-CFD and 1D-SCM. The mapping can be formulated on steady state conditions, as steady state reactive simulations do not require large computational effort for a 3D-CFD case. This methodology is demonstrated using the geometry (Fig 3.1) and DOC kinetics (Table 3.1).

A matrix of test case for mapping consisting of ten temperatures and four GHSVs is used as the test matrix to perform reactive steady state 3D-CFD simulations. Species conversion of the three species namely, CO, C_3H_6 and NO were chosen as candidates for the objective function. The mixed cup average values of the velocity at the catalyst inlet were used as starting guess for the nonlinear least squares optimization process. 1D-SCM solution was sought at the temperatures, with these velocities and inlet concentration as input to the 1D-SCM. The optimization solver `lsqnonlin` iterates until the error of the objective function is minimum. Temperature matrix consists of ten temperatures from 350 K to 575 K in 25K intervals. Light-off temperatures of the three species are within this temperature range. Four GHSVs were chosen to represent low and high velocities. The summary of the procedure is shown in Figure 4.14.

The value of mixed cup velocity at the inlet plane of the catalyst is used as the initial guess in the nonlinear least squares optimization. The desired conversions of the three species were obtained from the outlet plane of the catalyst. `lsqnonlin` was run for all the 40 operating points and the corresponding velocity of the pseudo-channel is plotted against the mixed cup inlet velocity as shown in Figure 4.15. The values of the three models and the corresponding velocities at inlet an outlet can be tabulated as look-up table, in addition to the plot in as shown in Figure 4.15.

From the Figure 4.15, we can see that the pseudo-channel is well correlated with the inlet mixed cup velocity of the 3D-CFD. Thus, a one-parameter model can adequately explain the flow maldistribution effects providing equivalent conversion of a 3D-CFD. The pseudo-channel also needs to have a smaller velocity for increased residence time to convert the species equal to 3D-CFD values. With different initial guesses, the model converged to the same end result, assuring unique solution for a set of temperature and conversion values in the objective function.

4.5.2 Performance of pseudo-channel under steady state reactive simulations

The performance of pseudo-channel is compared with that of 3D-CFD and 1D-SCM in terms of outlet temperature and species conversion. Light-off trends of temperature matched well with the CFD trends. The temperatures were slightly overestimated in the SCM and pseudo-channel cases, as the thermal mass is lumped and the radial heat transfer is not accounted in terms of solid conduction. However, species conversion values matched more closely with the CFD values and are better than the SCM results, for CO, C_3H_6 and NO. Figure 4.16 shows the comparison of performance of pseudo-channel in terms of NO conversion versus CFD and 1D-SCM results. One other observation is that the senstivity of the model with respect to temperature. As temperature varies

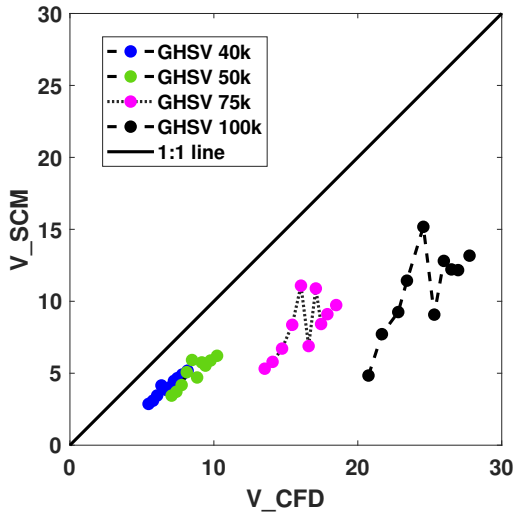

Figure 4.15: *Mapping of velocity of the pseudo-channel with the corresponding mixed cup inlet velocity from 3D-CFD simulations.*

from 375 K to 575 K, the species light-off of CO, followed by C_3H_6 occur and NO has a maximum conversion and the reversible oxidation to NO_2. As one of the species is completely converted, this species does not contribute to the gradients of the objective function, yet the pseudo-channel clearly predicts the values and trends of conversion and light-off temperatures. The model is effective in predicting the steady state results.

4.5.3 Performance of pseudo-channel under transient reactive simulations

After assessing the effectiveness of the pseudo-channel model, the subsequent step involves evaluating its performance during transitions between steady states, specifically in terms of velocity and temperature. In this regard, the transient analysis examines the response to step changes in both parameters at 2 seconds. Specifically, the velocity undergoes a step increase from 0.018 kg/s to 0.028 kg/s, while maintaining a constant temperature of 475 K. Similarly, the temperature experiences a step rise from 375 K to 475 K, with the mass flowrate held constant at 0.028 kg/s throughout.

The results of velocity step transient show that the performance of the pseudo-channel is better than the conventional SCM model in terms of outlet temperature. The species conversion predictions of the pseudochannel closely align with the CFD results, and the timing of the step change is accurately captured as a sharp jump in the values. Furthermore, the pseudo-channel values match very closely with 3D-CFD predictions both before and after the step, significantly outperforming the conventional SCM.

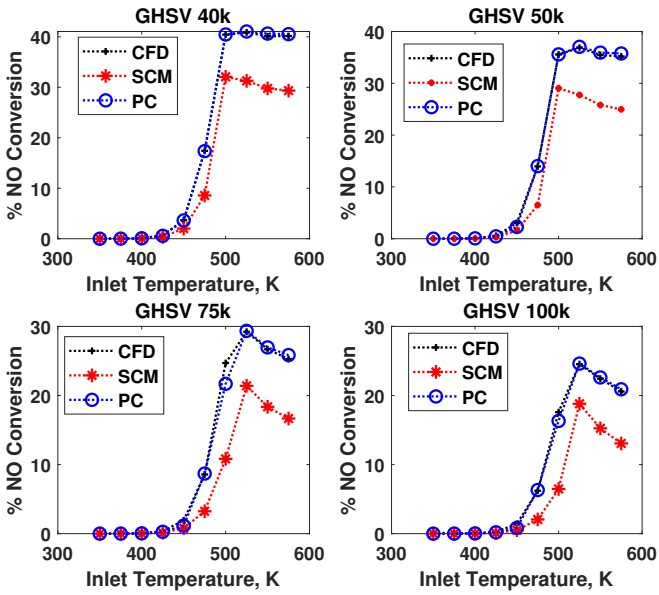

Figure 4.16: *Comparison of performances of 3D-CFD, 1D-SCM and pseudo-channel in terms of C_3H_6 conversion at the catalyst outlet in steady state reactive simulations.*

As observed in the velocity transients, the pseudo-channel predictions agree well with 3D-CFD predictions both before and after the step and is significantly better than conventional SCM for the temperature transients too, as shown in Figure 4.17. An interesting feature is the thermal lag behaviour. One would expect that 1D-SCM variants will have faster response than the CFD. The order of lag between the CFD and SCM variants is of the order of ten seconds. The dynamic response is a natural outcome of the 3D-CFD model as the radial heat conduction is well accounted for. The thermal mass is lumped in terms of the SCM variants and is not sensitive to the dynamic response of the changing temperature. This implies that as the inlet temperature changes, the CFD model is sensitive enough to predict the variation and retention times and the change is felt sooner than the SCM variants. However, due to the larger thermal mass, the final temperature attained is lower than the SCM variants. Thus, a one-parameter model is inadequate to capture the variation in retention times and sensitivity of temperature changes.

4.5.4 Computational Efficiency

An i7 processor powered desktop computer with 64 GB RAM was used for all simulations, both 1D-SCM and 3D-CFD. Simulations of reactive steady states were performed progressively from low temperatures (350K) to high temperatures (575K). The initialization was performed at 350K, and the converged solutions were then used for the next higher temperature setting, to reduce the CFD simulation times. Initially, the steady

Table 4.6: Comparative computational costs for steady state and transient simulations and other associated processing steps.

Details	3D-CFD	1D-SCM	Pseudo-Channel
Steady state reactive simulation	30 minutes	2 minutes	2 minutes
`lsqnonlin`	NA	5 minutes	NA
Transient reactive simulations	3 hours	5 minutes	5 minutes

state solutions were obtained in 18 minutes; however, the time to obtain steady state solutions for other temperatures was of the order of 30 minutes (the longer simulation times at higher temperatures are due to stiff kinetics. The solver `ode15s` in MATLAB and `lsqnonlin` were used to obtain the species conversions in the 1D-SCM and perform the mapping using nonlinear least squares optimization. The simulation time for the 1D-SCM cases were of the order of 2 minutes. Mapping procedure using nonlinear least squares was completed in 2-5 minutes for low temperatures (temperatures less than 450K) and high temperatures respectively (temperatures from 450K). The simulation duration for the 1D-SCM instances averaged around 2 minutes. The mapping process using nonlinear least squares took between 2 to 5 minutes, depending on whether the temperatures were low (below 450K) or high (450K and above). The computational time is shown in Table 4.6. As illustrated in Table 4.6, the ratio of computational times between CFD and the pseudo-channel SCM stands at $10^2 : 1$, offering versatile applications such as virtual calibration platforms, monitoring, and control [92].

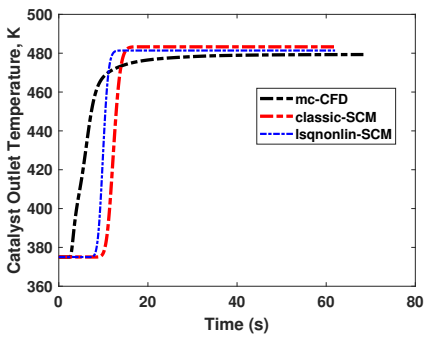

(a) *Temperature at the catalyst outlet*

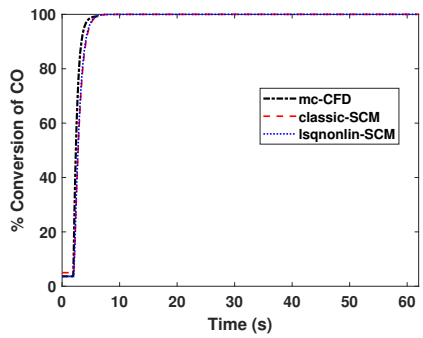

(b) *CO conversion at the catalyst outlet*

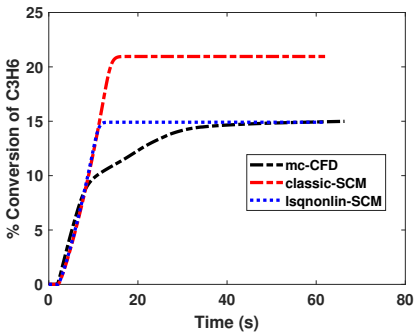

(c) *C_3H_6 conversion at the catalyst outlet*

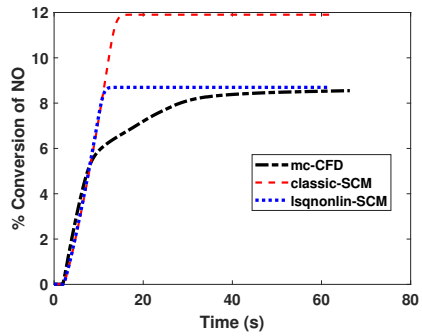

(d) *NO conversion at the catalyst outlet*

Figure 4.17: *Comparison of performances of 3D-CFD, 1D-SCM and pseudo-channel in terms outlet temperature and species conversions for a transient temperature step at the inlet.*

5 Conclusions and Future Work

5.1 Conclusions

In Paper I, a procedure was developed to understand and analyse the flow distribution in the academic muffler, using transient non-reactive simulations. To this end, a geometry with bend and a partial dead volume is chosen to study the flow profiles in the academic muffler. Two different transients were used, to understand the evolution of the uniformity index when the system moves from steady state to another steady state. Histograms and contours were used to demonstrate the non-uniform distribution of temperature and velocity in both the simulations. Pathlines also demonstrated that the few fluid streams had travelled longer paths than some of the other fluid streams in the muffler. Another interesting result was that the value of temperature uniformity index was dependent on the definition of temperature that was used as the flow variable. Scaled temperature values with different scaling were used to evaluate temperature uniformity index. A value of 0.95 for uniformity index in temperature and velocity do not mean the same level of distribution of velocity and temperature. The temperature field evolution is slower than the velocity field because of the larger thermal mass. The temperature field influences the velocity field through the change in fluid properties. The main outcome of the study is the validity of single channel model in the presence of flow maldistribution, as the flow in such devices under transient and even steady state conditions are very complex. This study can be used to build reduced order 3D models.

The conversion in EATS is influenced by the fluctuations and pulsations in the flow to the inlet of EATS. This is the focus of Paper II. A simple reactor geometry with a catalyst is used in this study. The geometry gas cones at the inlet and outlet, these create environments for mixing. Transient reactive simulations are performed with four different inlet velocities, namely, constant, pulse, sinusoidal and triangular ramp forcing functions. It was found that the time-averaged conversions and uniformity indices are dependent on the specifications of the inlet velocity. In a reactive case, the pulsations influences the retention time in the catalyst. The retention time distribution is influenced by flow distribution in the EATS. The mixed cup conversion is found to be a function of the inlet pulsations. The nature of the transient inlet velocities influences the dispersion of the gases in the catalyst. Fluctuations in temperature also affect the reaction rates. Reaction rate is non-linearly dependent on temperature. This dependence is altered by the fluctuations in the transient inlet conditions. When the inlet velocity is specified as a pressure value, flow discontinuity propagation is minimized. The mixing in the cones is also influenced by the fluctuations.

The validity of RANS simulations is checked using DES in Paper III. Unlike RANS, the large-scale turbulence is resolved in space and time in DES. The uniformity indices at various planes in the DES showed fluctuations, which could be significant during catalyst light-off behavior. However, the computational cost of DES is significantly higher by three orders of magnitude than that of RANS.

In Paper IV, a methodology was illustrated for the development of a multi-channel model for catalytic converters through the integration of multivariate data analysis techniques such as Principal Component Analysis (PCA) and D-optimal design, along with weighted least-squares regression from a CFD solution set. To demonstrate and evaluate the performance of the multi-channel model, a diesel oxidation catalyst with diverging cones and axisymmetry serves as the base model. A set of five reactions covering nine species was used in the reactive transient simulations. A porous media approximation was used to represent the catalyst. Transient profiles of mass flowrate, temperature and species concentration were applied at the inlet and the solution variables were collected at the outlet. A calibration case and three test cases were used in model order reduction procedure. The calibration dataset was rearranged and scaled for applying chemometric techniques. Five components were sufficient to explain most of the variance in the solution data. The D-optimal design procedure applied to the scores of the selected principal components determined the locations of the channels in the outlet plane. Out of the five channels identified through the D-optimal design, three were positioned closer to the wall, while one was situated at the center and another in the interior. Performances were compared in terms of the root mean square of the error of the objective functions, through weighted least squares regression. The performances of multi-channel model of all the test cases compared closer to the CFD results than the SCM, which cannot adequately capture spatio-temporal variations in inlet conditions arising from flow maldistribution. The computational effort needed to develop the multichannel model is similar to that of SCM, assuming the base CFD data is accessible.

As the procedure identifies the number of channels and their respective locations, it is possible to run SCM for these specific locations. The inlet conditions are identical for reactive and non-reactive cases. However, these channels then need to be combined using weights to get the model of the whole catalytic converter. One approach could be to use the temperature profiles of these channels and the mixed cup temperatures as the prediction set. The exotherms from the reactions alter the functional forms of the objective function. For example, the heat content is a monotonic function of the velocity and temperature, whereas conversion has a different functional form, with the same variables velocity and temperature. Alternatively, one can think of using steady state non-reactive simulations. Here, the variable that provides variance information for the PCA is velocity alone as heat effects do not influence the steady state results. These factors limit the use of chemometric modeling using non-reactive simulations for reduced-order model.

Multi-channel model developed in Paper IV showed improved performance than a 1D-SCM. However, this method needs large dataset for the chemometric analysis. Transient 3D-CFD simulations provide the base dataset for MVDA consuming huge computational load. 1D-SCM being advantageous with lower computational load, is less accurate as the thermal interactions and radial heat transfer are not modelled. These affect the performance of realistic systems with flow maldistribution. Steady state reactive 3D-CFD simulations are cheaper in terms of computational load. These also hold the information of flow maldistribution.

In Paper V, steady state reactive 3D-CFD simulations are used to map the 3D-CFD simulations with 1D-SCM. A pseudo-channel model is a fictitious SCM that will represent the operation of a realistic catalytic converter. To obtain the residence time or the velocity, steady state CFD results can be used to formulate an objective function, which would deliver the same conversion as the 3D-CFD. To this end, steady state conversion values are obtained at different GHSV, holding temperature constant. This helps to identify "the parameter(s)" required for formulating for the pseudo-channel. The computational costs associated with the pseudo-channel model are of the same order as the 1D-SCM. Performance assessment of this model is compared with the 3D-CFD solutions and the conventional SCM results, with steady state and transient test cases with velocity step and temperature step cases. In all the cases, the performance of the pseudo-channel model is significantly better than the conventional SCM model. Pseudo-channel model results agree very closely with the 3D-CFD results for steady state conditions and for velocity transient case. However, the sensitivity to capturing variation in retention times in a temperature step is limited due to lumping of thermal mass and absence of radial heat transfer modeling. The final steady states predicted by the pseudo-channel agree well with the 3D-CFD results. There is no restriction in terms of temperature ranges of velocity values in obtaining a stable, converged optimal value from `lsqnonlin` function. This model seems to be promising for other EATS like TWC and SCR. For systems involving multiphysics phenomena like evaporation and reaction, as in the SCR, a more detailed kinetic model needs to be used in the base CFD. For example, there can be accumulation of ammonia by adsorption on the monolith walls, leading to stiff changes in temperature and NOx conversion. In these cases, a microkinetic model solved by CFD solution can provide the base results for nonlinear least squares optimization.

5.2 Reflections from the results

Throughout this thesis, 3D-CFD simulations played a central role, both with and without reactions. As we know, 3D-CFD simulations offer great accuracy, but they come with a trade-off: extensive computation times. This limitation restricts their practical use in real-time applications such as hardware-in-the-loop testing, on-board diagnostics, and control operations in EATS. The primary motivation was to develop computationally efficient, yet accurate models derived from the detailed 3D-CFD simulations. To achieve this, techniques like chemometrics and nonlinear optimization were employed to create reduced-order models. These models significantly reduce computational load while maintaining fidelity. The benchmarking of the reduced-order models, *viz.,* the multi-channel model and the pseudo-channel model — revealed their suitability for real-time applications. Additionally, the thesis also explored how multivariate data analysis (MVDA) and optimization techniques could be combined with 3D-CFD solutions to obtain flow field variables at the catalyst outlet, in realistic systems with flow maldistribution. In summary, the thesis work aspires to provide systematic methodology to create reduced order models for systems with flow maldistribution.

5.3 Future work

The current work is focused on understanding flow distribution in EATS and developing reduced order models from 3D-CFD simulations.

To validate simulation results, measured flow field data is essential. Thermal data and velocity data can be obtained from thermocouples, Prandtl tube measurements, and hot wire anemometry. Laser techniques, such as Particle Image Velocimetry (PIV) and NO-LIF, can be used to provide velocity and concentration data. Additionally, LIF (Laser-Induced Fluorescence) can yield temperature measurements. By applying laser techniques, we can assess flow information at the monolith inlet, providing information about flow maldistribution.

This work can be extended to other EATS like SCR and ASC. Performance of SCR is dependent on the mixing of the sprays and the hydrolysis of urea to produce ammonia. The developed method of CFD simulations with chemometric techniques can be used to elucidate better injection locations and conditions. This information will be helpful for improved performance of SCR systems and optimise the performance of ASC.

Flow maldistribution is pronounced in EATS used in marine vessels owing to their large capacity engine exhausts. Scrubbers with amine solution of alkali solutions are used to convert CO_2, SOx and NO_x. A uniform spray enhances the efficiency of the scrubbers. It would be interesting to investigate this methodology for optimizing the sprays for effective conversion of the exhaust gases from a marine vessel.

6 Contribution to the field

This main contribution of this work can be summarized as:

6.1 Paper I

"Transient predictions of flow uniformity evolution in realistic exhaust gas aftertreatment systems using 3D-CFD"

The main contributions of this work is the demonstration of the limitations of SCM via histogram representation of velocity and temperature and the evolution of uniformity index when a system moves between two states. This work is one of the fewer works that addresses flow distribution under transient and non-reactive conditions. The role of thermal mass and pressure drop in the flow uniformity evolution are also studied. This analysis is a potential way to develop reduced order 1D+ models. I performed all the simulations and wrote the first draft of the paper. I performed the analysis and evaluation of the results together with my co-authors.

6.2 Paper II

"Numerical assessment of flow pulsation effects on reactant conversion in automotive monolithic reactors"

The influence of pulsations and fluctuations on the time-averaged conversion and time-averaged uniformity index are studied. This study showed that even with the same time-averaged inlet velocity, there are stark differences in the time-averaged outlet conversion. I performed all the simulations and prepared the results for the draft. I together with my advisors, evaluated the results and analysed them.

6.3 Paper III

"Turbulent uniformity fluctuations in automotive catalysts–A RANS vs DES assessment"

CFD simulations were performed on geometry with bends. Uniformity indices were predicted for DES turbulence models and were compared with RANS results. DES provides turbulent UI fluctuations that were not resolved using RANS, this could be significant for the catalyst light-off behavior. I with my advisors developed the project. I performed simulations with other authors. I performed the analysis and evaluation of the results together with my co-authors. I wrote the first draft of the paper.

6.4 Paper IV

"Methodology for reduced-order multi-channel modeling of a catalytic converter"

A reduced order model for an oxidation catalyst was developed through the application of multivariate data analysis methods (PCA, D-Optimal Design and Weighted least squares) on transient reactive CFD simulation output. Performance of test cases were compared against the SCM in terms of residuals and RMSE. This methodology integrates CFD models with chemometric techniques to develop multi-channel models. I performed all the simulations, prepared the results for the draft, and wrote the first draft of the paper. I performed the analysis and evaluation of the results together with my co-authors.

6.5 Paper V

"A reduced-order pseudo-channel model accounting for flow maldistribution in automotive catalysis"

Predictions of conversion for reactive simulations for systems with flow maldistribution were made by developing a pseudo-channel concept. The residence time of the equivalent pseudo-channel was obtained by nonlinear least squares mapping of species conversions between CFD and SCM simulations at steady state temperatures and inlet velocities. In terms of species conversion, the performance of the pseudo-channel was assessed for both steady-state and transient test cases. In all the test cases, pseudo-channel predictions were in close agreement with the CFD simulations. The methodology aimed at obtaining reduced-order models for catalytic converters with flow maldistribution from steady-state simulations. I performed all the simulations and prepared the results for the draft. I together with my advisors, evaluated the results and analyzed them. I wrote the first draft of the paper.

Bibliography

[1] *IPCC, 2023: Climate Change 2023: Synthesis Report. Contribution of Working Groups I, II and III to the Sixth Assessment Report of the Intergovernmental Panel on Climate Change [Core writing team, H. Lee and J. Romero (eds.)]. IPCC, Geneva, Switzerland*. Tech. rep. July 2023. DOI: https://doi.org/10.59327/IPCC/AR6-9789291691647.

[2] *World's first year-long breach of key 1.5 °C warming limit — bbc.com*. https://www.bbc.com/news/science-environment-68110310. last accessed on 2024-05-12.

[3] John B Heywood. *Internal combustion engine fundamentals*. McGraw-Hill Education, 2018.

[4] İbrahim Aslan Reşitoğlu, Kemal Altinişik, and Ali Keskin. "The pollutant emissions from diesel-engine vehicles and exhaust aftertreatment systems". In: *Clean Technologies and Environmental Policy* 17.1 (2015), pp. 15–27.

[5] *History of CARB*. last accessed on 2024-05-12. URL: https://ww2.arb.ca.gov/about/history.

[6] *EU: Cars and Light Trucks*. last accessed on 2024-05-12. URL: https://dieselnet.com/standards/eu/ld.php.

[7] *EU: Cars and Light Trucks: RDE Testing*. last accessed on 2024-05-12. URL: https://dieselnet.com/standards/eu/ld_rde.php.

[8] Stacy C Davis and Robert Gary Boundy. *Transportation energy data book: Edition 39*. Tech. rep. Oak Ridge National Lab.(ORNL), Oak Ridge, TN (United States), 2021.

[9] *Euro 7: Council adopts new rules on emission limits for cars, vans and trucks*. last accessed on 2024-05-12. URL: https://www.consilium.europa.eu/en/press/press-releases/2024/04/12/euro-7-council-adopts-new-rules-on-emission-limits-for-cars-vans-and-trucks/.

[10] Jan Kašpar, Paolo Fornasiero, and Neal Hickey. "Automotive catalytic converters: current status and some perspectives". In: *Catalysis today* 77.4 (2003), pp. 419–449.

[11] Ronald M Heck, Robert J Farrauto, and Suresh T Gulati. *Catalytic air pollution control: commercial technology*. John Wiley & Sons, 2016.

[12] *Emission Control Technologies*. last accessed on 2024-05-12. URL: https://dieselnet.com/tech/engine_emission-control.php.

[13] Jerzy Merkisz, Piotr Bielaczyc, Jacek Pielecha, and Joseph Woodburn. *RDE testing of passenger cars: The effect of the cold start on the emissions results*. Tech. rep. SAE Technical Paper, 2019.

[14] Robert E Hayes and Stan T Kolaczkowski. *Introduction to catalytic combustion*. Routledge, 2021.

[15] Olaf Deutschmann. "Modeling of the interactions between catalytic surfaces and gas-phase". In: *Catalysis Letters* 145 (2015), pp. 272–289.

[16] *Catalytic Converters*. last accessed on 2024-05-12. URL: `https://dieselnet.com/tech/cat_conv.php`.

[17] Calvin H Bartholomew and Robert J Farrauto. *Fundamentals of industrial catalytic processes*. John Wiley & Sons, 2011.

[18] Matthias Hettel, Eric Daymo, Tobias Schmidt, and Olaf Deutschmann. "CFD-Modeling of fluid domains with embedded monoliths with emphasis on automotive converters". In: *Chemical Engineering and Processing-Process Intensification* 147 (2020), p. 107728.

[19] Anna Holmgren, Thomas Grönstedt, and Bengt Andersson. "Improved flow distribution in automotive monolithic converters". In: *Reaction Kinetics and Catalysis Letters* 60.2 (1997), pp. 363–371.

[20] Mingfei Mu, Xinghu Li, Jawad Aslam, Yong Qiu, Hao Yang, Guiyue Kou, and Yan Wang. "A study of shape optimization method on connection cones for diesel particulate filter (DPF)". In: *ASME International Mechanical Engineering Congress and Exposition*. Vol. 50664. American Society of Mechanical Engineers. 2016, V012T16A001.

[21] Mingfei Mu, Jonas Sjöblom, Henrik Ström, and Xinghu Li. "Analysis of the flow field from connection cones to monolith reactors". In: *Energies* 12.3 (2019), p. 455.

[22] Mingfei Mu, Jonas Sjöblom, Nikhil Sharma, Henrik Ström, and Xinghu Li. "Experimental study on the flow field of particles deposited on a gasoline particulate filter". In: *Energies* 12.14 (2019), p. 2701.

[23] Leonardo Giani, Gianpiero Groppi, and Enrico Tronconi. "Mass-transfer characterization of metallic foams as supports for structured catalysts". In: *Industrial & engineering chemistry research* 44.14 (2005), pp. 4993–5002.

[24] ANSYS FLUENT. *R2021 Theory Guide-1.2 Continuity and Momentum Equations*. 2021.

[25] Gaurav Agrawal, Niket S Kaisare, S Pushpavanam, and Karthik Ramanathan. "Modeling the effect of flow mal-distribution on the performance of a catalytic converter". In: *Chemical engineering science* 71 (2012), pp. 310–320.

[26] Achuth Munnannur, Christopher M Cremeens, and Z Gerald Liu. “Development of Flow Uniformity Indices for Performance Evaluation of Aftertreatment Systems”. In: *SAE International Journal of Engines* 4.1 (2011), pp. 1545–1555.

[27] Zeynep Ilsen Önsan and Ahmet Kerim Avci. *Multiphase catalytic reactors: Theory, design, manufacturing, and applications*. John Wiley & Sons, 2016.

[28] Abhishek Suman, Nikhil Dilip Khedkar, Asish Kumar Sarangi, and Jose Martin Herreros. “Numerical modelling and non-dimensional analysis of a diesel oxidation catalyst with focus on NO2 reduction”. In: *International Journal of Engine Research* (2024), p. 14680874241228950.

[29] Ali Hussain Motagamwala and James A Dumesic. “Microkinetic modeling: a tool for rational catalyst design”. In: *Chemical Reviews* 121.2 (2020), pp. 1049–1076.

[30] Larry C Young and Bruce A Finlayson. “Mathematical models of the monolith catalytic converter: Part I. Development of model and application of orthogonal collocation”. In: *AIChE Journal* 22.2 (1976), pp. 331–343.

[31] Larry C Young and Bruce A Finlayson. “Mathematical models of the monolith catalytic converter: Part II. Application to automobile exhaust”. In: *AIChE Journal* 22.2 (1976), pp. 343–353.

[32] Se H Oh and James C Cavendish. “Transients of monolithic catalytic converters. Response to step changes in feedstream temperature as related to controlling automobile emissions”. In: *Industrial & Engineering Chemistry Product Research and Development* 21.1 (1982), pp. 29–37.

[33] JHBJ Hoebink, RA Van Gemert, JAA Van Den Tillaart, and GB Marin. “Competing reactions in three-way catalytic converters: modelling of the NOx conversion maximum in the light-off curves under net oxidising conditions”. In: *Chemical Engineering Science* 55.9 (2000), pp. 1573–1581.

[34] R Holder, M Bollig, DR Anderson, and JK Hochmuth. “A discussion on transport phenomena and three-way kinetics of monolithic converters”. In: *Chemical engineering science* 61.24 (2006), pp. 8010–8027.

[35] LS Mukadi and RE Hayes. “Modelling the three-way catalytic converter with mechanistic kinetics using the Newton–Krylov method on a parallel computer”. In: *Computers & chemical engineering* 26.3 (2002), pp. 439–455.

[36] Louise Olsson, Björn Westerberg, Hans Persson, Erik Fridell, Magnus Skoglundh, and Bengt Andersson. “A kinetic study of oxygen adsorption/desorption and NO oxidation over Pt/Al2O3 catalysts”. In: *The Journal of Physical Chemistry B* 103.47 (1999), pp. 10433–10439.

[37] RE Hayes, B Liu, and M Votsmeier. “Calculating effectiveness factors in non-uniform washcoat shapes”. In: *Chemical Engineering Science* 60.7 (2005), pp. 2037–2050.

[38] H Santos and M Costa. “Modelling transport phenomena and chemical reactions in automotive three-way catalytic converters”. In: *Chemical Engineering Journal* 148.1 (2009), pp. 173–183.

[39] S Siemund, JP Leclerc, D Schweich, M Prigent, and F Castagna. “Three-way monolithic converter: simulations versus experiments”. In: *Chemical Engineering Science* 51.15 (1996), pp. 3709–3720.

[40] Björn Lundberg, Jonas Sjoblom, Åsa Johansson, Björn Westerberg, and Derek Creaser. “Parameter estimation of a DOC from engine rig experiments with a discretized catalyst washcoat model”. In: *SAE International Journal of Engines* 7.2 (2014), pp. 1093–1112.

[41] Björn Lundberg, Jonas Sjöblom, Åsa Johansson, Björn Westerberg, and Derek Creaser. “DOC modeling combining kinetics and mass transfer using inert washcoat layers”. In: *Applied Catalysis B: Environmental* 191 (2016), pp. 116–129.

[42] M Walander, J Sjöblom, D Creaser, B Lundberg, S Tamm, and J Edvardsson. “Efficient experimental approach to evaluate mass transfer limitations for monolithic DOCs”. In: *Topics in Catalysis* 62 (2019), pp. 391–396.

[43] Petr Kočí, Miloš Marek, Milan Kubíček, Teuvo Maunula, and Matti Härkönen. “Modelling of catalytic monolith converters with low-and high-temperature NOx storage compounds and differentiated washcoat”. In: *Chemical Engineering Journal* 97.2-3 (2004), pp. 131–139.

[44] N Mladenov, J Koop, S Tischer, and O Deutschmann. “Modeling of transport and chemistry in channel flows of automotive catalytic converters”. In: *Chemical Engineering Science* 65.2 (2010), pp. 812–826.

[45] Saurabh Y. Joshi, Michael P. Harold, and Vemuri Balakotaiah. “On the use of internal mass transfer coefficients in modeling of diffusion and reaction in catalytic monoliths”. In: *Chemical Engineering Science* 64.23 (2009), pp. 4976–4991. ISSN: 00092509. DOI: 10.1016/j.ces.2009.08.008.

[46] D Papadias, L Edsberg, and P Björnbom. “Simplified method of effectiveness factor calculations for irregular geometries of washcoats: A general case in a 3D concentration field”. In: *Catalysis Today* 60.1-2 (2000), pp. 11–20.

[47] M Walander, J Sjöblom, D Creaser, B Agri, N Löfgren, S Tamm, and J Edvardsson. “Modelling of Mass Transfer Resistances in Non-uniformly Washcoated Monolith Reactors”. In: *Emission Control Science and Technology* 7.2 (2021), pp. 153–162.

[48] Henrik Ström and Srdjan Sasic. “Heat and mass transfer in automotive catalysts—The influence of turbulent velocity fluctuations”. In: *Chemical engineering science* 83 (2012), pp. 128–137.

[49] Nikunj Gupta and Vemuri Balakotaiah. “Heat and mass transfer coefficients in catalytic monoliths”. In: *Chemical Engineering Science* 56.16 (2001), pp. 4771–4786.

[50] H Weltens, H Bressler, F Terres, H Neumaier, and D Rammoser. “Optimization of catalytic converter gas flow distribution by CFD distribution”. In: *SAE paper* 930780 (1993).

[51] MEei Hong, Li Chengyue, Liu Hui, and Ji Shengfu. “Simulation of catalytic combustion of methane in a monolith honeycomb reactor”. In: *Chinese Journal of Chemical Engineering* 14.1 (2006), pp. 56–64.

[52] Ankan Kumar and Sandip Mazumder. “Toward simulation of full-scale monolithic catalytic converters with complex heterogeneous chemistry”. In: *Computers & chemical engineering* 34.2 (2010), pp. 135–145.

[53] GC Koltsakis, PA Konstantinidis, and AM Stamatelos. “Development and application range of mathematical models for 3-way catalytic converters”. In: *Applied Catalysis B: Environmental* 12.2-3 (1997), pp. 161–191.

[54] Julia Windmann, Joachim Braun, Peter Zacke, Steffen Tischer, Olaf Deutschmann, and Jürgen Warnatz. “Impact of the inlet flow distribution on the light-off behavior of a 3-way catalytic converter”. In: *SAE transactions* (2003), pp. 713–723.

[55] Gaurav Agrawal, Niket S Kaisare, S Pushpavanam, and Karthik Ramanathan. “Modeling the effect of flow mal-distribution on the performance of a catalytic converter”. In: *Chemical engineering science* 71 (2012), pp. 310–320.

[56] Sruti Dammalapati, Preeti Aghalayam, and Niket Kaisare. “Modeling the Effects of the Inlet Manifold Design on the Performance of a Diesel Oxidation Catalytic Converter”. In: *Industrial & Engineering Chemistry Research* 60.10 (2021), pp. 3860–3870.

[57] Zhi Liu, Stephen F Benjamin, and Carol A Roberts. *Pulsating flow maldistribution within an axisymmetric catalytic converter-flow rig experiment and transient cfd simulation*. Tech. rep. SAE Technical Paper, 2003.

[58] Ivan Cornejo, Petr Nikrityuk, and Robert E Hayes. “Pressure correction for automotive catalytic converters: A multi-zone permeability approach”. In: *Chemical Engineering Research and Design* 147 (2019), pp. 232–243.

[59] VK Chakravarthy, JC Conklin, CS Daw, and EF D’Azevedo. “Multi-dimensional simulations of cold-start transients in a catalytic converter under steady inflow conditions”. In: *Applied Catalysis A: General* 241.1-2 (2003), pp. 289–306.

[60] Jana Aslanjan, Christian Klauer, Vivien Günther, and Fabian Mauß. “Simulation of a three-way catalyst using a transient multi-channel model”. In: *Digital Proceedings of the 8th European Combustion Meeting (ECM 2017), Dubrovnik, Croatia*. 2017, pp. 570–574.

[61] Paolo Canu and S Vecchi. “CFD simulation of reactive flows: Catalytic combustion in a monolith”. In: *AIChE Journal* 48.12 (2002), pp. 2921–2935.

[62] Ivan Cornejo, Petr Nikrityuk, and Robert E Hayes. “Turbulence generation after a monolith in automotive catalytic converters”. In: *Chemical Engineering Science* 187 (2018), pp. 107–116.

[63] Ivan Cornejo, Petr Nikrityuk, and Robert E Hayes. “Turbulence decay inside the channels of an automotive catalytic converter monolith”. In: *Emission Control Science and Technology* 3 (2017), pp. 302–309.

[64] James C Sutherland and Alessandro Parente. “Combustion modeling using principal component analysis”. In: *Proceedings of the Combustion Institute* 32.1 (2009), pp. 1563–1570.

[65] Gianmarco Aversano, Aurélie Bellemans, Zhiyi Li, Axel Coussement, Olivier Gicquel, and Alessandro Parente. “Application of reduced-order models based on PCA & Kriging for the development of digital twins of reacting flow applications”. In: *Computers & chemical engineering* 121 (2019), pp. 422–441.

[66] Jonas Sjöblom. *Parameter estimation in heterogeneous catalysis*. Chalmers Tekniska Hogskola (Sweden), 2009.

[67] Frank M White and Joseph Majdalani. *Viscous fluid flow*. Vol. 3. McGraw-Hill New York, 2006.

[68] Suhas V Patankar. *Numerical heat transfer and fluid flow*. CRC press, 2018.

[69] Henk Kaarle Versteeg and Weeratunge Malalasekera. *An introduction to computational fluid dynamics: the finite volume method*. Pearson education, 2007.

[70] JN Reddy. *An introduction to the finite element method*. Vol. 1221. McGraw-Hill New York, 2004.

[71] Stephen B Pope. *Turbulent flows*. Cambridge: Cambridge Univ. Press, 2011.

[72] David C Wilcox et al. *Turbulence modeling for CFD*. Vol. 2. DCW industries La Canada, CA, 1998.

[73] Charles G Speziale. “On turbulent secondary flows in pipes of noncircular cross-section”. In: *International Journal of Engineering Science* 20.7 (1982), pp. 863–872.

[74] Florian R Menter. “Two-equation eddy-viscosity turbulence models for engineering applications”. In: *AIAA journal* 32.8 (1994), pp. 1598–1605.

[75] A Pandya, J Mmbaga, RE Hayes, W Hauptmann, and M Votsmeier. “Global kinetic model and parameter optimization for a diesel oxidation catalyst”. In: *Topics in Catalysis* 52 (2009), pp. 1929–1933.

[76] Michael Greenacre, Patrick JF Groenen, Trevor Hastie, Alfonso Iodice d’Enza, Angelos Markos, and Elena Tuzhilina. “Principal component analysis”. In: *Nature Reviews Methods Primers* 2.1 (2022), p. 100.

[77] Karl Pearson. “LIII. On lines and planes of closest fit to systems of points in space”. In: *The London, Edinburgh, and Dublin philosophical magazine and journal of science* 2.11 (1901), pp. 559–572.

[78] Lennart Eriksson, Tamara Byrne, E Johansson, Johan Trygg, and C Vikström. *Multi-and megavariate data analysis basic principles and applications*. Vol. 1. Umetrics Academy, 2013.

[79] Ian T Jolliffe and Jorge Cadima. “Principal component analysis: a review and recent developments”. In: *Philosophical transactions of the royal society A: Mathematical, Physical and Engineering Sciences* 374.2065 (2016), p. 20150202.

[80] Thomas Minka. “Automatic choice of dimensionality for PCA”. In: *Advances in neural information processing systems* 13 (2000).

[81] Richard Cangelosi and Alain Goriely. “Component retention in principal component analysis with application to cDNA microarray data”. In: *Biology direct* 2.1 (2007), pp. 1–21.

[82] Friedrich Pukelsheim. *Optimal design of experiments*. SIAM, 2006.

[83] P Fernandes de Aguiar, B Bourguignon, MS Khots, DL Massart, and R Phan-Than-Luu. “D-optimal designs”. In: *Chemometrics and intelligent laboratory systems* 30.2 (1995), pp. 199–210.

[84] Douglas C Montgomery, Elizabeth A Peck, and G Geoffrey Vining. *Introduction to linear regression analysis*. John Wiley & Sons, 2021.

[85] *The NIPALS Algorithm*. last accessed on 2024-05-12. URL: `https://cran.r-project.org/web/packages/nipals/vignettes/nipals_algorithm.html`.

[86] *candexch*. last accessed on 2024-05-12. URL: `https://se.mathworks.com/help/stats/candexch.html`.

[87] Robert J Kee, Michael E Coltrin, and Peter Glarborg. *Chemically reacting flow: theory and practice*. John Wiley & Sons, 2005.

[88] HS Fogler. *Elements of Chemical Reaction*. Pearson Education, 2020.

[89] Kenneth Levenberg. “A method for the solution of certain non-linear problems in least squares”. In: *Quarterly of applied mathematics* 2.2 (1944), pp. 164–168.

[90] Donald W Marquardt. “An algorithm for least-squares estimation of nonlinear parameters”. In: *Journal of the society for Industrial and Applied Mathematics* 11.2 (1963), pp. 431–441.

[91] *lsqnonlin*. last accessed on 2024-05-12. URL: `e.mathworks.com/help/optim/ug/lsqnonlin.html`.

[92] Ethan Faghani, Jelena Andric, and Jonas Sjoblom. “Toward an effective virtual powertrain calibration system”. In: *SAE Technical Paper* 2018-01-0007 (2018).

Appendix - I

Experimental features and modeling methodology are described in this chapter. For further information, publications I and II can be referred to. The construction of the experiment rig along with its associated instrumentation are presented in this section.

A1.1 Experimental Rig

The EATS rig used in this study is designed to capture the relevant features of an industrial EATS fitted in a vehicle, that it should have bend and/or a dead volume, that creates a recirculation zone. The experimental rig should also be operated in transient condition. The rig should also operate under cold and warm conditions. Figure 6.1 shows the experimental rig.

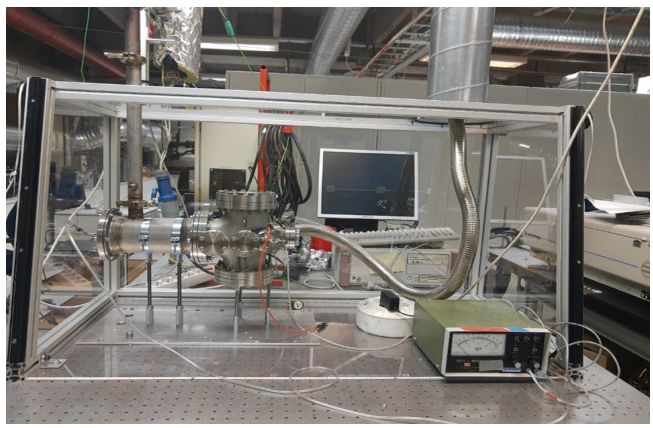

Figure A1.1 Experimental Rig

The experimental rig is called as "Academic Muffler". It has a vertical section and a horizontal section. The vertical section has the inlet port. The vertical section is fitted with a catalyst that acts as a flow straightener. The section is long enough so that the flow is fully developed in the vertical section. The inlet section is 3 cm in internal diameter and 50 cm long. The material of construction is stainless steel (SS310). The horizontal section is connected to the vertical section by a 90° bend. The right side of the horizontal section houses the catalyst.

The catalyst is a diesel oxidation catalyst (DOC). This is kept insulated by layers of glass wool. The dimensions of the catalyst are 9.5 cm in diameter and 15 cm in length.

This is the main catalyst. The inlet pipe is also fitted with a small catalyst, that serves to dampen the flow. This small catalyst is also wrapped inside layers of insulation.

The muffler is provided with ports for the passage of working fluids. The working fluids are air and nitric oxide. Air is the working fluid for flow and temperature profile visualization. Nitric oxide (NO) gas along with air will be used for species profile visualization. Air is injected from the vertical section, whereas small circular nozzles in the horizontal will be the entry port for nitric oxide. The role of nitric oxide is more of a tracer that will be illuminated via laser to get concentration profiles in the catalyst. Expanding mat is used to hold the catalyst in place and to minimize heat losses.

A1.2 Associated Instrumentation

Three mass flow controllers (MFC) of capacities 1000 slpm, 200 slpm and 2 slpm (Bronkhorst) are used to regulate the flowrate of air, diluent air and nitric oxide gas respectively. The flowrates are specified at STP [1]. K-type thermocouples are inserted at the front and rear ends of the catalyst in the horizontal section to measure temperatures in the channels of the monolith. Three more thermocouples are placed on the vertical pipe for further measurements that are required for controlling the temperature and tuning the heat transfer coefficients. The fluids that are used in the experiment are heated by using a Eurotherm fitted with controllers for close control of temperatures. Positive drought is ensured for flow of gases from the muffler, by calibrating the pressure drop across the ventilation lines. The data acquisition is accomplished by in-house LabVIEW module. This also helps in running automated flow experiments. the muffler is attached to an optically active chamber for use of laser diagnostics. Gaskets and seals used in the muffler and optical chamber are chosen that they are compatible with NO gas. The experimental rig is enclosed in a ventilated hood.

The nitric oxide gas cylinders are stored in gas cabinets that can withstand high temperature for a period of 90 minutes. The gas line is secured with multiple regulators and non-return valves for safe flow of nitric oxide. Leak alarms are placed inside the hood and in the experimental area. This is because the allowable leak for NO gas is very stringent.

A1.3 Calibration Experiments

Pressure drop in the horizontal section was measured by manometer by varying the flowrate at the inlet. This information is required in the porous media to specify the resistance to the flow in the monolith in the simulations.

[1] Standard Temperature and Pressure (STP) 273.15 K and 101.325 kPa

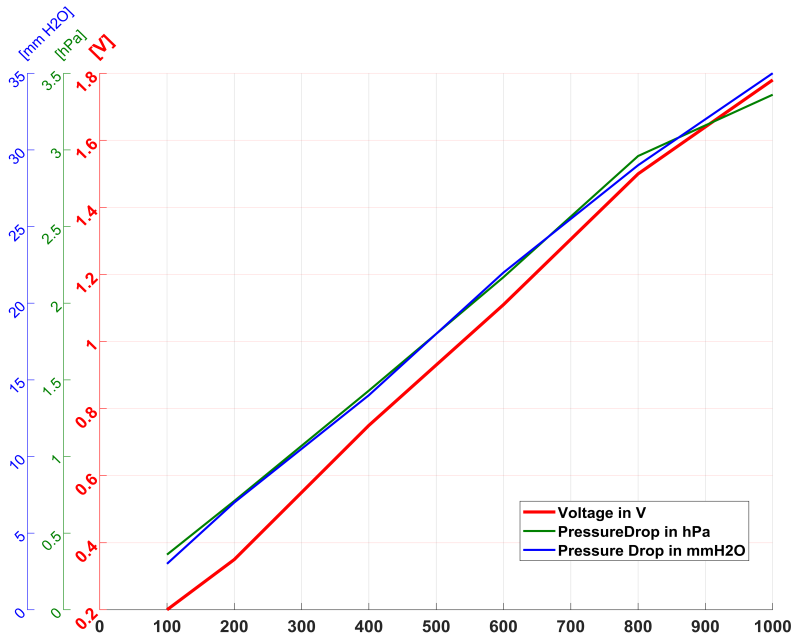

Figure A1.2 Pressure drop Vs Flowrate Calibration